nature neuroscience

ARTICLES

https://doi.org/10.1038/s41593-022-01138-x

Preconfigured dynamics in the hippocampus are guided by embryonic birthdate and rate of neurogenesis

Roman Huszár[1,2] ✉, Yunchang Zhang[1,2], Heike Blockus[3,4] and György Buzsáki[1,2,5] ✉

The incorporation of new information into the hippocampal network is likely to be constrained by its innate architecture and internally generated activity patterns. However, the origin, organization and consequences of such patterns remain poorly understood. In the present study we show that hippocampal network dynamics are affected by sequential neurogenesis. We birthdated CA1 pyramidal neurons with in utero electroporation over 4 embryonic days, encompassing the peak of hippocampal neurogenesis, and compared their functional features in freely moving adult mice. Neurons of the same birthdate displayed distinct connectivity, coactivity across brain states and assembly dynamics. Same-birthdate neurons exhibited overlapping spatial representations, which were maintained across different environments. Overall, the wiring and functional features of CA1 pyramidal neurons reflected a combination of birthdate and the rate of neurogenesis. These observations demonstrate that sequential neurogenesis during embryonic development shapes the preconfigured forms of adult network dynamics.

The hippocampus plays a crucial role in the rapid encoding and storage of episodic memories. This function is thought to depend on its unique anatomical and functional organization[1]. In contrast to the neocortex where receptive fields are topographically organized (that is, physically nearby neurons have similar fields), hippocampal 'place cells' that represent the same or different parts of an environment are thought to be randomly distributed throughout the hippocampus[2,3]. It has been suggested that the specific constellation of place cells representing a particular environment is established via activity-dependent plasticity[4], which allows the expression of place fields at arbitrary locations. The anatomical organization of the CA3 recurrent system is assumed to form a large random graph[1,5], endowing the hippocampus with a large storage capacity. Based on these anatomical and physiological observations, theoretical and computational models of hippocampal function have been developed using a framework consisting of randomly connected uniform principal neurons[6].

However, several considerations point to the oversimplicity of plasticity-based reorganizations to a randomly connected network and, instead, indicate that hippocampal principal cells are organized into heterogeneous, parallel circuit modules, enhancing computational flexibility and supporting a rich repertoire of behaviors. In the narrow CA1 pyramidal layer, the sole corticofugal output of the hippocampus, important differences have been noted in the septotemporal, mediolateral and radial organization. Gene expression, intrinsic physiological features, short- and long-range connectivity and place field properties vary with anatomical position within the pyramidal layer[7–15]. Recent work also indicates that this rich heterogeneity is coupled with a preservation of the individual properties of neurons and their assembly cooperation. The number of hippocampal place fields is strongly skewed at the population level and remarkably stable across environmental conditions and time at the single-cell level[16]. Place field emergence is biased toward locations with weak subthreshold drive[17] and is predictable from a pre-existing correlation structure[18–20]. These recent observations lead to an alternative view that structural organization in hippocampal networks gives rise to a reservoir of preconfigured activity patterns, which are available for matching with new experiences[18,19,21]. A potential source of these pre-existing states is embryonic development[22,23].

To address the origin of the functional heterogeneity and preconfigured dynamics in the adult brain, we probed the functional consequences of developmental events that take place before behavioral experience. To examine how intrauterine development affects future hippocampal function, we birthdated CA1 pyramidal neurons with in utero electroporation at four embryonic stages, and performed high-density silicon probe recordings to compare their functional features in freely moving, adult mice. In contrast to neurons born on different days, same-birthdate pyramidal neurons exhibited prominent coactivity across brain states and a stronger preservation of overlapping place fields across different environments. Spatial representations were topographically organized in same-birthdate populations, in that anatomically clustered (<500-μm) neurons were functionally related. With the aid of a computational model, we show that pre-existing correlations between same-birthdate neurons interact with the rate of neurogenesis to shape the diversity of observed assembly patterns. Same-birthdate neurons exhibited strong convergence on to local interneurons, suggesting a microcircuit basis for our results. Altogether, our findings demonstrate that sequential neurogenesis in embryonic development guides the preconfigured forms of adult hippocampal networks.

Results

In vivo recordings from birthdated CA1 pyramidal neurons. To label CA1 pyramidal neurons with distinct birthdates, we performed in utero electroporation of ChR2-enhanced yellow fluorescent protein (eYFP) and tdTomato in mouse embryos at four prenatal stages (Fig. 1a and Extended Data Fig. 1; Methods). To validate the temporal specificity of induced expression, 5-bromo-2′-deoxyuridine

[1]Neuroscience Institute, New York University, New York, NY, USA. [2]Center for Neural Science, New York University, New York, NY, USA. [3]Department of Neuroscience, Columbia University, New York, NY, USA. [4]Zuckerman Mind Brain Behavior Institute, Columbia University, New York, NY, USA. [5]Department of Neurology, Langone Medical Center, New York, NY, USA. ✉e-mail: roman.huszar.17@gmail.com; gyorgy.buzsaki@nyulangone.org

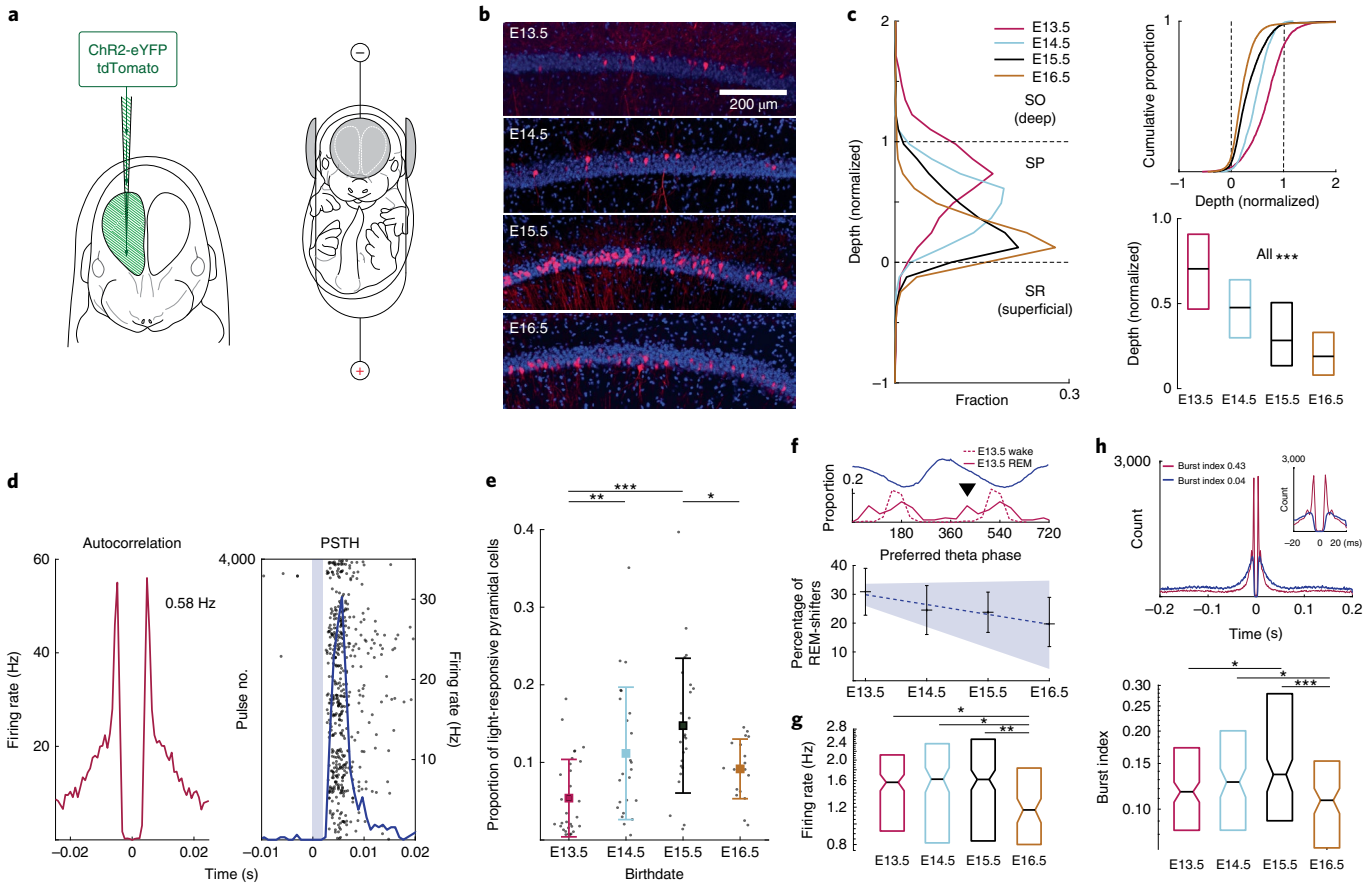

Fig. 1 | In vivo characterization of birthdated pyramidal neurons in mouse hippocampus. a, Schematic of in utero electroporation of plasmids (ChR2-eYFP and tdTomato) for birthdating CA1 pyramidal neurons. **b**, The tdTomato expression resulting from in utero electroporation at four embryonic (E) dates: E13.5, E14.5, E15.5 and E16.5. **c**, Left: radial depth distributions across birthdates (Methods; Extended Data Fig. 1b); right: cumulative distributions and box plots of radial depth distributions: E13.5, 0.71 (n = 2,657 tdTomato$^+$ puncta); E14.5, 0.48 (n = 1,993); E15.5, 0.28 (n = 7,749); E16.5, 0.19 (n = 9,173). Median, Kruskal–Wallis test: $H = 4.5 \times 10^3$, degrees of freedom (d.f.) = 3, $P = 0$. SO = stratum oriens ; SP = stratum pyramidale; SR = stratum radiatum. **d**, Left: spike autocorrelogram of a pyramidal neuron identified on the basis of waveform shape and bursting statistics; right: raster plot of the neuron's responses to optogenetic stimulation (2 ms, shaded blue) and superimposed PSTH (blue curve). **e**, Proportion of light-responsive pyramidal cells per recording session[24]: E13.5, 5.39 ± 5% (n = 30 sessions); E14.5, 11.16 ± 8.5% (n = 24); E15.5, 14.74 ± 8.7% (n = 24); E16.5, 9.16 ± 3.8% (n = 18); mean ± s.d., ANOVA: $F(3,92) = 8.525$, $P = 4 \times 10^{-4}$. **f**, Top: distribution of preferred theta phases of E13.5 pyramidal neurons (n = 95) during waking and REM sleep. Blue trace shows mean LFP from two consecutive theta cycles. Arrowhead: REM sleep-induced theta-phase shift. Bottom: fraction of theta-modulated light-responsive cells that shifted their phase to the peak of theta in REM sleep: E13.5, 30.89% (n = 123 modulated neurons); E14.5, 24.5% (n = 106); E15.5, 23.8% (n = 143); E16, 19.7% (n = 76). Slope of regression line = −3.42%, $P = 0.028$ (bootstrap, one tailed). Black crosses: mean ± 95% bootstrapped confidence interval (CI). Blue line and shading: linear regression ± 95% bootstrapped CI. **g**, Firing rate distributions across birthdates: E13.5, 1.57 Hz (n = 184 neurons); E14.5, 1.63 Hz (n = 132); E15.5, 1.62 Hz (n = 233); E16.5, 1.16 Hz (n = 115). Median, Kruskal–Wallis test: $H = 11.8186$, d.f. = 3, $P = 1.6 \times 10^{-2}$. **h**, Top: autocorrelograms of example pyramidal neurons with similar firing rates but different burst propensities; bottom: burst indices (spike count at 2- to 5-ms lags normalized by count at 200- to 300-ms lags) across birthdates: E13.5, 0.1167 (n = 184 neurons); E14.5, 0.1272 (n = 132); E15.5, 0.136 (n = 233); E16.5 = 0.1082 (n = 115). Median, Kruskal–Wallis test: $H = 13.87$, d.f. = 3, $P = 4.4 \times 10^{-3}$. $^*P < 0.05$, $^{**}P < 0.01$, $^{***}P < 0.001$. Box plot's central mark, notch and edges indicate the median, its 95% CI and the 25th/75th percentiles, respectively. See Supplementary Table 3 for P values of multiple comparisons.

(BrdU) was injected into pregnant dams at varying times around electroporation, confirming that labeling was largely confined to neurons born on the same day (Extended Data Fig. 1). In adult brains, pyramidal neurons born on embryonic (E) days 13.5, 14.5, 15.5 and 16.5 occupied broadly overlapping, yet distinct, sublayers spanning the deep-to-superficial axis of the pyramidal layer (Fig. 1b,c)[22]. To investigate the dynamics of birthdated pyramidal neurons in vivo, adult mice that underwent electroporation at different embryonic stages (E13.5, n = 4; E14.5, n = 3; E15.5, n = 6; E16.5, n = 4; Supplementary Table 1) were implanted with high-density silicon probes and optic fibers targeting CA1. Pyramidal neurons were separated from interneurons based on waveform shape and bursting statistics (Extended Data Fig. 2a,b). Birthdated pyramidal neurons were identified optogenetically by reliable, short-latency discharge following 1.5- to 3-ms light pulses (Fig. 1d and Extended Data Fig. 2; Methods). Waveform shapes of light-responsive pyramidal neurons were no different from those of nonresponsive neurons (Extended Data Fig. 2i). Furthermore, light-evoked spikes were systematically most similar to spontaneous spikes of their assigned cluster (Extended Data Fig. 2d–f), validating our identification method of birthdated pyramidal cells in vivo.

The fraction of light-responsive pyramidal neurons at each birthdate was consistent with the previously observed, bell-shaped wave of hippocampal neurogenesis peaking between E14 and E15 (Fig. 1e)[24,25]. Earlier born pyramidal neurons had higher firing rates (Fig. 1g) and received the strongest drive from the entorhinal cortex,

as reflected indirectly by the largest fraction of pyramidal neurons with a theta-phase preference that shifted in rapid eye movement (REM) sleep (Fig. 1f)[8,12,13]. In contrast, the propensity to fire in bursts displayed an inverted-U function of birthdate (Fig. 1h). This nonlinear relationship suggests a potential decoupling of the effect of anatomical positioning in the pyramidal layer from the effect of birthdate-related physiological parameters (Extended Data Fig. 3).

Cofiring of SBD pyramidal neurons in all brain states. Given their common input from CA3 pyramidal neurons[25,26], we hypothesized that same-birthdate (SBD) pyramidal neurons would form functionally compact microcircuits exhibiting structured (co)activity. To explore this idea, we studied pairwise and single-neuron firing patterns while animals dwelled in their homecage ($n=15$ animals, Supplementary Table 1).

As for burst firing (Fig. 1h), single-cell statistics exhibited a nonlinear (U or inverted-U)-shaped relationship with birthdate. During theta oscillations, intermediate birthdate pyramidal neurons (E14.5 and E15.5) locked to a broader range of theta phases (that is, lower depth modulation) in the waking, but not the REM, state (Fig. 2d). Sharp-wave ripple SPW-R-related firing rates and participation probability also exhibited an inverted-U-shaped relationship with birthdate (Fig. 2f). Consistent with previous reports[22], these differences could not solely be explained by the estimated anatomical depth of pyramidal neurons (Extended Data Fig. 3 and Supplementary Table 2).

Crosscorrelograms (CCGs) of spike trains recorded in the homecage pointed to greater synchrony between pairs of SBD than different-birthdate (DBD) pyramidal neurons (Fig. 2a), an observation that was prominent individually in 11 of 13 animals (Fig. 2b and Extended Data Fig. 4). To investigate the brain state dependence of this coactivity, we focused on the firing statistics of pyramidal neurons during theta oscillations (active wake) and SPW-Rs (quiet wake/non-REM (NREM) sleep). SBD pyramidal neurons exhibited greater pairwise correlations than DBD neurons in both individual theta cycles (Fig. 2c) and SPW-Rs (Fig. 2e,g), suggesting a brain state-independent mechanism. These results depended on neither firing rate nor cluster isolation quality differences (Extended Data Fig. 5).

Birthdated neurons join assemblies with distinct dynamics. Given the cofiring statistics of SBD pyramidal neurons and differences in single-cell features across birthdates, we hypothesized that SBD pyramidal neurons would join cell assemblies with birthdate-dependent dynamics. To study cell assemblies, we performed independent component analysis (ICA) on the *z*-scored spike matrix of pyramidal neurons to extract patterns of higher-order cofiring (Fig. 3a,b)[27]. Pyramidal neurons with large independent component (IC) weights (>2 s.d.) were considered to be assembly members and individual assemblies were grouped by the birthdate of their members (Methods). To study the structure of assembly dynamics, we focused on SPW-Rs, which engage large fractions of pyramidal neurons to fire. Pairs of assembly members cofired in SPW-Rs more prominently than pairs of assembly nonmembers (Fig. 3c). Similar to the single-cell firing features, assembly member cofiring with assembly nonmembers depended nonlinearly on birthdate. Specifically, firing patterns of pyramidal neurons that were members of assemblies associated with earliest (E13.5) and latest (E16.5) birthdates were the most segregated (lowest correlation) from the firing patterns of assembly nonmembers (Fig. 3c). To further explore the heterogeneity of assembly activity, we obtained time-resolved estimates of assembly expression by projecting each independent component on to the *z*-scored spike matrix (Fig. 3d). Timestamps associated with significant peaks in the resulting time-series were considered moments of assembly expression and analyzed further (Methods). Assemblies were expressed in SPW-Rs at rates that depended nonlinearly on assembly member birthdate (Fig. 3e). In particular, assemblies with members born at intermediate birthdates (E14.5) were expressed at higher rates than those with members born earlier (E13.5) and later (E16.5).

The above observations are consistent with the possibility that birthdated pyramidal neurons are biased to fire in SPW-R-related assemblies made up of other SBD pyramidal neurons. To detect assemblies associated with the spiking of a held-out birthdated pyramidal neuron, we identified its spikes in SPW-Rs and performed ICA on the remaining pyramidal neurons in the corresponding time bins (Extended Data Fig. 6a and Methods). Compared with assemblies comprising exclusively DBD neurons, assemblies comprising other SBD pyramidal neurons were more likely to be expressed surrounding the SPW-R-related spikes of held-out neurons (Extended Data Fig. 6b). Moreover, held-out neurons exhibited higher SPW-R-related pairwise cofiring with assembly members than with nonmembers and their cofiring with SBD assembly members was the strongest (Extended Data Fig. 6c).

Last, SPW-R-related coactivation of larger groups of light-responsive neurons was studied explicitly, both in the context of the ICA analysis framework described above (Extended Data Fig. 7a,b) and in terms of coactivation probabilities for fixed subgroups of SBD neurons (Extended Data Fig. 7c–e). In each case, larger groups (more than two neurons) of SBD neurons exhibited a greater propensity for coactivation compared with control groups of equal size.

Cofiring of SBD neurons interacts with rates of neurogenesis. The temporal profile of assembly expression rates (Fig. 3e)

Fig. 2 | Theta- and SPW-R-related cofiring of same-birthdate pyramidal neurons. a, Left: *z*-scored CCGs for pairs of SBD and DBD pyramidal neurons recorded in an example animal electroporated at E13.5. Bold lines are averages across pairs ($n=977$ and $n=13{,}198$, respectively), and thin lines are ten example pairs from each group. Right: the difference between mean *z*-scored CCGs pointing to larger synchrony in the SBD group. **b**, Difference between average *z*-scored CCGs between SBD and DBD pairs for each animal (row). Two E13.5 animals were excluded due to a lack of SBD pairs. White dotted lines indicate the median duration of SPW-Rs across all recordings (36.4 ms). (See Extended Data Fig. 4 for individual animal statistics.) **c**, Left: example raster and LFP showing cofiring of SBD pyramidal neurons (PYR) (blue) in the same theta cycle; right: pairwise spike count correlations in theta cycles between SBD (blue, median = 0.0189; $n=3{,}751$) and DBD pairs (red, median = 0.0087; $n=50{,}461$; $P=9.98\times10^{-46}$; two-sided Wilcoxon's test). **d**, Theta-depth modulation of neurons across birthdates. Top: W: wake: E13.5, 0.127 ($n=178$ phase-locked neurons); E14.5, 0.099 ($n=127$); E15.5, 0.094 ($n=207$); E16.5, 0.103 ($n=101$). Medians, Kruskal–Wallis test: $H=63.3868$, d.f. = 3, $P=0$. Bottom: REM: E13.5, 0.1408 ($n=105$); E14.5, 0.128 ($n=99$); E15.5, 0.1414 ($n=118$); E16.5, 0.1423 ($n=73$). Medians, Kruskal–Wallis test: $H=3.077$, d.f. = 3, $P=5.46\times10^{-1}$. NS, not significant. **e**, Example LFP and raster showing cofiring of SBD (blue dots) and other pyramidal neurons during a hippocampal SPW-R (gray rectangle). **f**, Left: firing rates during SPW-Rs at different birthdates: E13.5, 7.8 Hz ($n=184$ neurons); E14.5, 8.75 Hz ($n=132$); E15.5, 8.01 Hz ($n=233$); E16.5, 6.13 Hz ($n=115$). Medians, Kruskal–Wallis test: $H=21.94$, d.f. = 3, $P=6\times10^{-0}$. Right: fraction of SPW-Rs with at least one spike from a light-responsive neuron across different birthdates: E13.5, 0.245 ($n=184$); E14.5, 0.268 ($n=132$); E15.5, 0.235 ($n=233$); E16.5, 0.194 ($n=115$). Medians, Kruskal–Wallis test: $H=19.4058$, d.f. = 3, $P=2\times10^{-4}$. **g**, Pairwise spike count correlation in SPW-Rs for SBD (blue, median = 0.0399; $n=3{,}751$ pairs) and DBD pairs (red, median = 0.0231; $n=50{,}461$; $P=3.96\times10^{-116}$; two-sided Wilcoxon's test). $^{\#}P<0.1$, $^{*}P<0.05$, $^{**}P<0.01$, $^{***}p<0.001$. Box plot's central mark, notch and edges indicate the median, its 95% CI and the 25th/75th percentiles, respectively. See Supplementary Table 3 for *P* values of multiple comparisons.

qualitatively resembled the bell-shaped wave of pyramidal neurons labeled at different birthdates (Fig. 1e). A potential explanation is that assembly dynamics and pairwise correlations are biased by intrinsic single-cell differences in SPW-R-related firing, which also exhibited a bell-shaped pattern with birthdate (Fig. 2f). An alternative explanation is that the rate of neurogenesis interacts with a correlation rule[28]. To distinguish between these hypotheses, we constructed a phenomenological model that allowed firing rates and pairwise correlations to be tuned independently (Fig. 4a,b and Extended Data Fig. 8a; Methods)[29]. The number of neurons was set to follow a bell-shaped function of birthdate ('bell-shaped' model; Fig. 1e and Extended Data Fig. 8b) and firing rates across birthdates were set according to empirically observed distributions in SPW-Rs (Fig. 2f and Extended Data Fig. 8c). When pairwise correlations between SBD neurons were absent, the bell-shaped model failed to generate assembly expression rates comparable to data (Fig. 4c,d). This suggests that the inverted-U-shaped pattern of firing rates is not sufficient. In contrast, as we increased the strength of correlations, the bell-shaped model generated assembly dynamics yielding a good match to

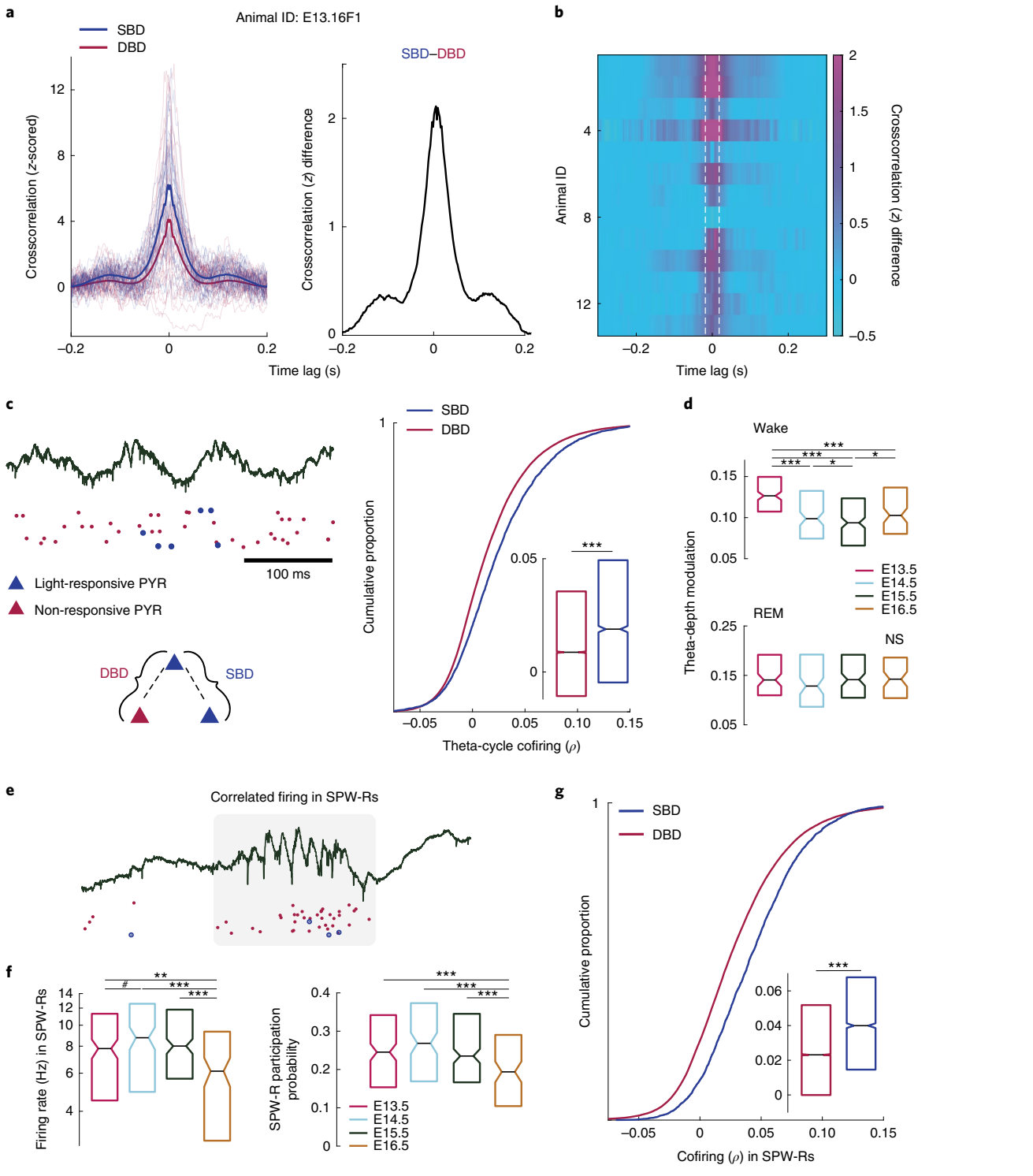

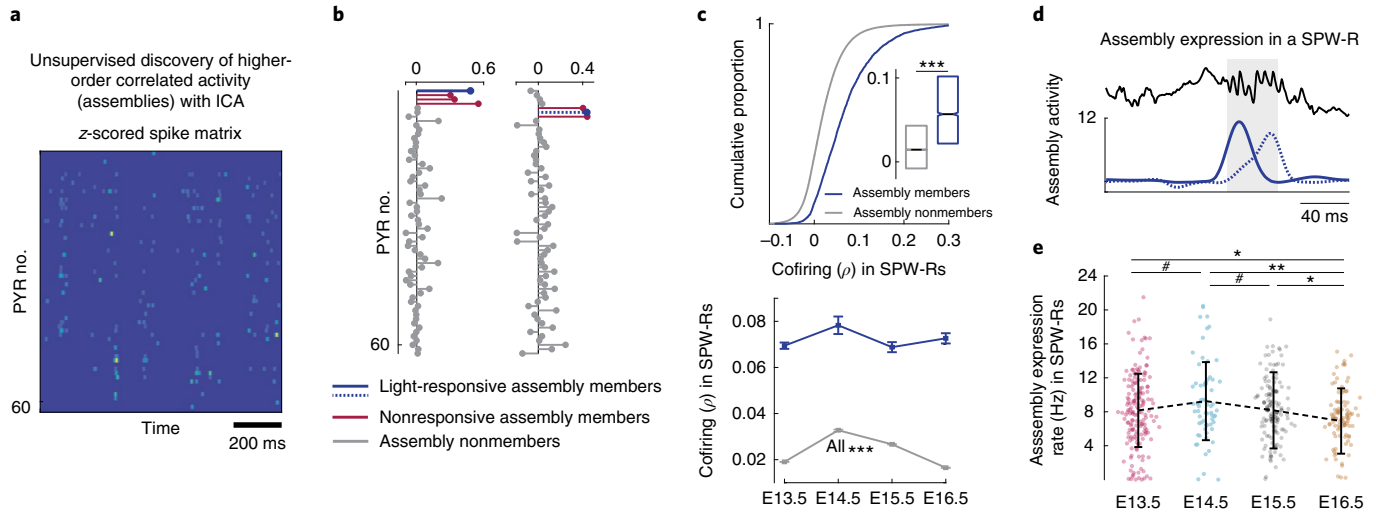

Fig. 3 | Distinct dynamics of cell assemblies with birthdated neuron members. a, Example *z*-scored spike matrix from 61 simultaneously recorded pyramidal neurons (PYR). ICA was performed to identify assemblies, groups of neurons displaying prominent coactivation[27]. **b**, Example weights associated with two ICs. Pyramidal neurons with weights exceeding 2 s.d. were considered to be assembly members. Blue indicates light-responsive (birthdated) assembly members, red nonresponsive assembly members and gray assembly nonmembers. **c**, Top: pairwise spike count correlations in SPW-Rs between members of the same assembly (blue, median = 0.0568; $n = 4{,}676$ pairs) and between assembly member and nonmember neurons (gray, median = 0.0145; $n = 199{,}139$; $P = 0$; two-sided Wilcoxon's test). Bottom: same as above, grouped by the birthdate of assembly members. Assembly member versus nonmember cofiring (gray): E13.5, $0.019 \pm 1.37 \times 10^{-4}$ ($n = 105{,}357$ pairs); E14.5, $0.033 \pm 4.1 \times 10^{-4}$ ($n = 12{,}398$); E15.5, $0.027 \pm 2.23 \times 10^{-4}$ ($n = 37{,}946$); E16.5, $0.016 \pm 2.1 \times 10^{-4}$ ($n = 43{,}438$). Mean ± s.e.m., ANOVA: $F(3{,}199{,}135) = 717.4478$, $P = 0$. **d**, Time-resolved assembly expression (colors identical to those of birthdated assembly members in **b)** during a SPW-R, resulting from the projection of ICs on to each column of the *z*-scored spike matrix. Significant peaks were taken as time points of assembly expression, resulting in a time series. **e**, Assembly expression rate in SPW-Rs for assemblies with birthdated assembly members: E13.5, 8.16 ± 4.3 ($n = 167$); E14.5, 9.25 ± 4.6 ($n = 67$); E15.5, 8.16 ± 4.49 ($n = 140$); E16.5, 6.9 ± 3.85 ($n = 97$). Mean ± s.d., ANOVA: $F(3{,}467) = 4.05$, $P = 1.58 \times 10^{-2}$. Dots denote individual assemblies. $^{\#}P < 0.1$, $^{*}P < 0.05$, $^{**}P < 0.01$, $^{***}P < 0.001$. Box plot's central mark, notch and edges indicate the median, its 95% CI and the 25th/75th percentiles, respectively. See Supplementary Table 4 for *P* values of multiple comparisons.

those observed in data (Fig. 4c,d and Extended Data Fig. 8d,e). To further probe the contribution of the bell-shaped rate of neurogenesis, we also employed a model with uniformly distributed neurons across birthdates ('uniform' model), which failed to capture assembly dynamics observed in data across all tested parameters (Extended Data Fig. 9). We leveraged the uniform model to generate a null distribution of error fits at each point of the parameter space, thereby obtaining a 'significance boundary' for the goodness of fit of the bell-shaped model (Methods; Fig. 4d, black line). This boundary suggests that reproducing the observed assembly patters requires correlations between neurons to decay at some minimum time constant of the difference of their birthdates (~2 h under the bell-shaped model; Fig. 4d). Overall, these results suggest that correlated activity between SBD neurons and a bell-shaped neurogenesis curve suffices to produce the assembly dynamics observed in data and offers a plausible mechanism for generating a diverse repertoire of assembly patterns.

SBD pyramidal neurons exhibit overlapping place tuning. As SBD neurons displayed structured cofiring during both SPW-Rs and theta oscillations, we investigated the consequences of such preconfigured dynamics on spatial receptive field tuning. We trained adult mice ($n = 9$; Supplementary Table 1) to perform a place alternation task in a familiar figure-eight maze with a 5-s delay between choices (Fig. 5a). During maze performance, the spatial information content of spikes (measured in bits per second and as the number of spatial bins with reliably high firing rate) was largest in pyramidal neurons with intermediate birthdates (E14.5 and E15.5; Fig. 5b). SBD neurons exhibited greater overlap in spatial tuning, as reflected by higher spatial ratemap correlations compared with DBD neurons (Fig. 5c and Extended Data Fig. 5e,j). Surprisingly, the strength of spatial ratemap correlations depended on the anatomical distance between SBD neurons, in that spatial ratemaps of SBD pyramidal neurons ≤250 µm apart exhibited systematically larger overlap than those of DBD neurons (Fig. 5d and Extended Data Fig. 10).

Changes in environmental context typically result in a global reorganization of spatial tuning. To explore this feature in birthdated populations, we compared their firing on the left and right arms of the figure-eight maze. Population firing rate vectors at linearized positions along the maze decorrelated between left and right trial types as soon as animals exited the common stem segment of the maze (Fig. 5e). Despite the different contexts between the two trial types, spatial ratemaps of SBD neurons tended to systematically reorganize closer together compared with those of DBD neurons (Fig. 5f).

To more rigorously assess the persistence of representational similarity among SBD neurons, we exposed a separate cohort of animals ($n = 3$; Supplementary Table 1) to a total of $n = 16$ novel environment exploration sessions (Fig. 6a,b). Individual pyramidal neurons preserved their theta-related firing rates across environments, although pairwise analysis revealed systematically higher spatial ratemap correlations in novel environments (Fig. 6c). This latter difference may be due to lower spatial information content in novel environments (Fig. 6d), which has previously been attributed to firing outside of the place field[30]. As in the familiar environment (Fig. 5c), SBD neurons exhibited higher spatial ratemap correlations compared with DBD neurons (Fig. 6e). This result was not dependent on differences in firing rate or cluster isolation quality (Extended Data Fig. 5k–p). Importantly, novel environment-related spatial ratemaps of SBD neurons tended to reorganize closer together compared with those of DBD neurons (Fig. 6a,b,f), which is consistent with biased spatial ratemap reorganization of SBD neurons across left and right arms of the familiar figure-eight maze (Fig. 5f).

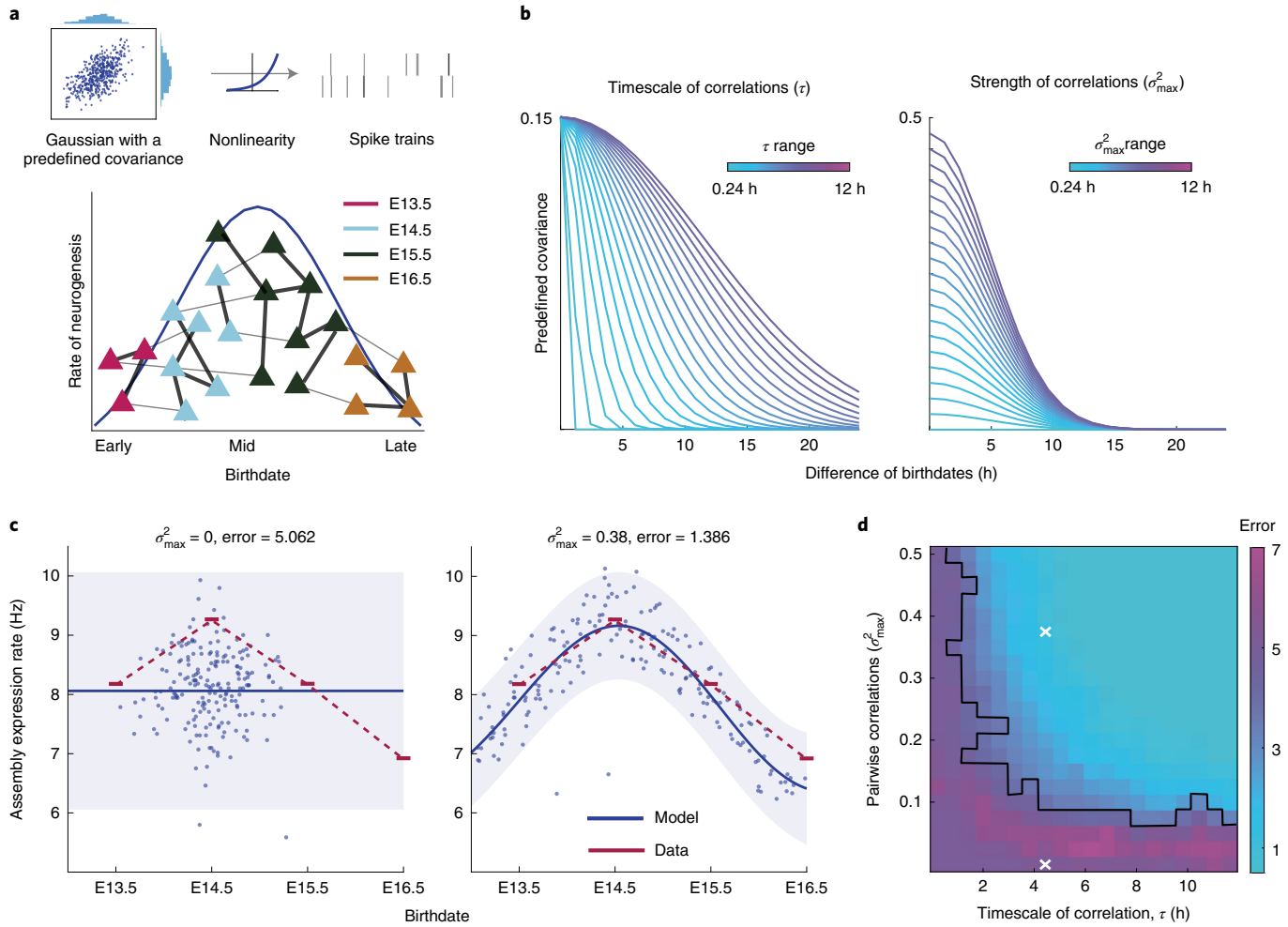

Fig. 4 | Correlations between SBD neurons interact with the rate of neurogenesis to produce the observed assembly dynamics. a, Top: schematic of a phenomenological model for exploring the statistical structure of assembly dynamics (Extended Data Fig. 8). Spikes were sampled from a transformed random process with tunable firing rates and correlations. Firing rates across birthdates were set according to distributions in SPW-Rs (Fig. 2f) and the strength of correlations was varied between simulations. Bottom: schematic illustrating a hypothesized effect of neurogenesis rate and stronger correlations among SBD neurons. Large neurogenesis rates give rise to more prominently expressed assemblies. Triangles represent pyramidal neurons and lines the strengths of pairwise correlations. **b**, Illustration of the effect of free parameters τ and σ^2_{max} on the predefined covariance (Methods). Left: as τ increases, covariance decays more slowly as the difference of birthdates (dob_{diff}) increases. Right: as σ^2_{max} increases, the covariance decays from a larger initial value. In short, σ^2_{max} sets the strength of covariance between SBD neurons, whereas τ controls the rate at which it decays as the difference of birthdates increases, and implicitly defines the window during which neurons must be born to exhibit pre-existing correlations. **c**, Simulated assembly expression rates at different birthdates ($n = 200$ assemblies, blue dots) yielded different qualitative fits to the observed assembly expression rates (red, average data as in Fig. 3e), depending on the strength of correlation σ^2_{max} between SBD neurons. The timescale of correlation parameter τ was constant in the two examples. Goodness of fit was assessed as the $-\log(P)$ of data under a nonlinear regression model summarizing the simulated assembly expression rates (blue line, posterior mean; shaded blue, posterior 95% CI; Methods). **d**, The $-\log(P)$ (error) matrix quantifying the model fit (as in **c**; $n = 200$ assemblies) as a function of the correlation strength (σ^2_{max}) and the timescale of correlation (τ). White crosses highlight examples in **c**. The black line separates a region of the parameter space (upper right) where the bell-shaped neurogenesis model performs significantly better than a uniform neurogenesis model (Extended Data Fig. 9).

Altogether, these results suggest that pre-existing correlations between SBD neurons manifest in a structured overlap of spatial representations and this bias persists in the face of changing environmental contexts.

The above observations are consistent with the possibility that birthdated pyramidal neurons are biased to fire in assemblies made up of other SBD pyramidal neurons during behavior. Similar to SPW-Rs (Extended Data Fig. 6a–c), we identified the assemblies of each held-out birthdated pyramidal cell by performing ICA on the remaining pyramidal cells at times of the held-out neuron's spikes on the familiar figure-eight maze (Extended Data Fig. 6d). We found that assemblies containing other SBD pyramidal neurons were more likely to be expressed surrounding the spikes of held-out neurons (Extended Data Fig. 6e), and their ratemaps overlapped more strongly with that of the held-out neuron (Extended Data Fig. 6f,g). Last, held-out pyramidal neurons cofired in theta cycles with assembly members more strongly than with assembly nonmembers and their cofiring with SBD assembly members was the strongest (Extended Data Fig. 6h).

Common birthdate shapes the structure of CA1 microcircuits. To identify a microcircuit-based explanation for the persistent neuronal interaction of SBD neurons across brain states and behavior, we examined local monosynaptic connectivity between

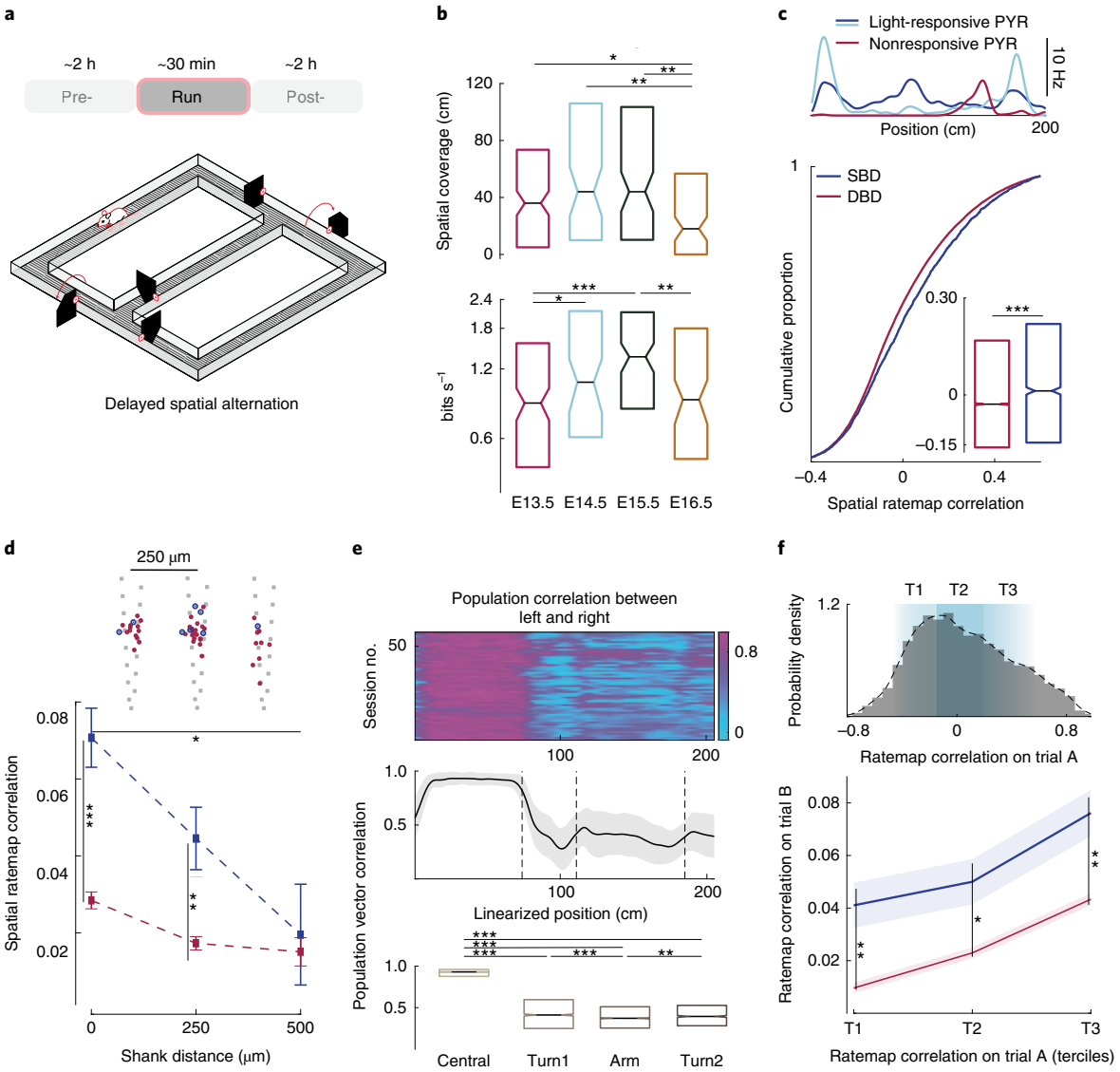

Fig. 5 | SBD neurons exhibit topographically organized spatial representations in familiar environments. a, Schematic of a figure-eight maze. Mice alternated between arms for water reward. **b**, Single-cell firing features during maze exploration. Top: spatial coverage (cm) with reliable (>1 bit cm^{-1}) high firing rate (>5 Hz): E13.5, 36 cm ($n=164$ neurons); E14.5, 44 ($n=76$); E15.5, 44 ($n=111$); E16.5, 18 ($n=115$). Medians, Kruskal–Wallis test: $H=13.99$, d.f. = 3, $P=6.2\times10^{-3}$. Bottom: spatial information in bits s^{-1}: E13.5, 0.836 ($n=164$ neurons); E14.5, 1.05 ($n=76$); E15.5, 1.35 ($n=111$); E16.5, 0.88 ($n=115$). Medians, Kruskal–Wallis test: $H=20.23$, d.f. = 3, $P=6\times10^{-4}$. **c**, Top: example spatial ratemaps of light-responsive (blue) and nonresponsive (red) neurons. Left and right arm ratemaps (excluding the central stem) were concatenated for every neuron. Spatial ratemap correlations between SBD (blue, median = 0.0152; $n=2{,}609$) and DBD (red, median = −0.0256, $n=39{,}965$) pairs ($P=1.86\times10^{-10}$; two-sided Wilcoxon's test). **d**, Spatial ratemap correlation as a function of shank distance of SBD (n = 2,561) and DBD (n = 38,619) pairs. Top: light-responsive (blue) and nonresponsive (red) neurons overlaid on the silicon probe recording sites (gray). Shank spacing was 250 μm. A two-way ANOVA revealed a main effect of common birthdate ($F(1,40{,}939)=16.97$, $P=0$), tercile ($F(2,40{,}939)=10.53$, $P=0$), but no interaction ($F(2,40{,}939)=2.98$, $P=5.1\times10^{-2}$). **e**, Population vector correlation between left and right trials as a function of the linearized position. Decorrelation following the central stem (common to left and right trials) reveals distinct representations: Central, 0.93 ($n=4{,}218$ population vector pairs); Turn1, 0.412 ($n=2{,}109$); Arm, 0.372 ($n=4{,}218$); Turn2, 0.3944 ($n=1{,}140$). Medians, Kruskal–Wallis test: $H=7{,}278.3$, d.f. = 3, $P=0$. **f**, Top: ratemap correlation distribution of SBD pairs, divided into terciles (T1–T3). Left and right trial ratemap correlations were calculated separately and pooled. Bottom: ratemap correlations in one trial type (left or right) as a function of the tercile in the other (right or left, respectively) for SBD ($n=5{,}137$) and DBD ($n=77{,}398$) pairs. A two-way ANOVA revealed a main effect of common birthdate ($F(1,81{,}197)=37.93$, $P=0$), tercile ($F(2,81{,}197)=16.79$, $P=0$), but no interaction ($F(2,81{,}197)=0.12$, $P=8.8\times10^{-1}$). $^{*}P<0.05$, $^{**}P<0.01$, $^{***}P<0.001$. All error bars = s.e.m. Box plot's central mark, notch and edges indicate the median, its 95% CI and the 25th/75th percentiles, respectively. See Supplementary Tables 4 and 5 for *P* values of multiple comparisons.

pyramidal neurons and putative interneurons (Fig. 7a)[31]. SBD pyramidal neuron pairs converged on to postsynaptic interneurons more strongly than DBD pairs (Fig. 7b). Furthermore, both pyramidal cell-to-interneuron convergence and the strength of effective synaptic coupling (spike transmission probability) showed a bell-shaped relationship with birthdate (Fig. 7c–e). Last, spike transmission probability peaked at presynaptic firing frequencies in the gamma range (15- to 23-ms presynaptic interspike intervals (ISIs); Fig. 7d,e), a timescale associated with assembly organization in the hippocampus[32].

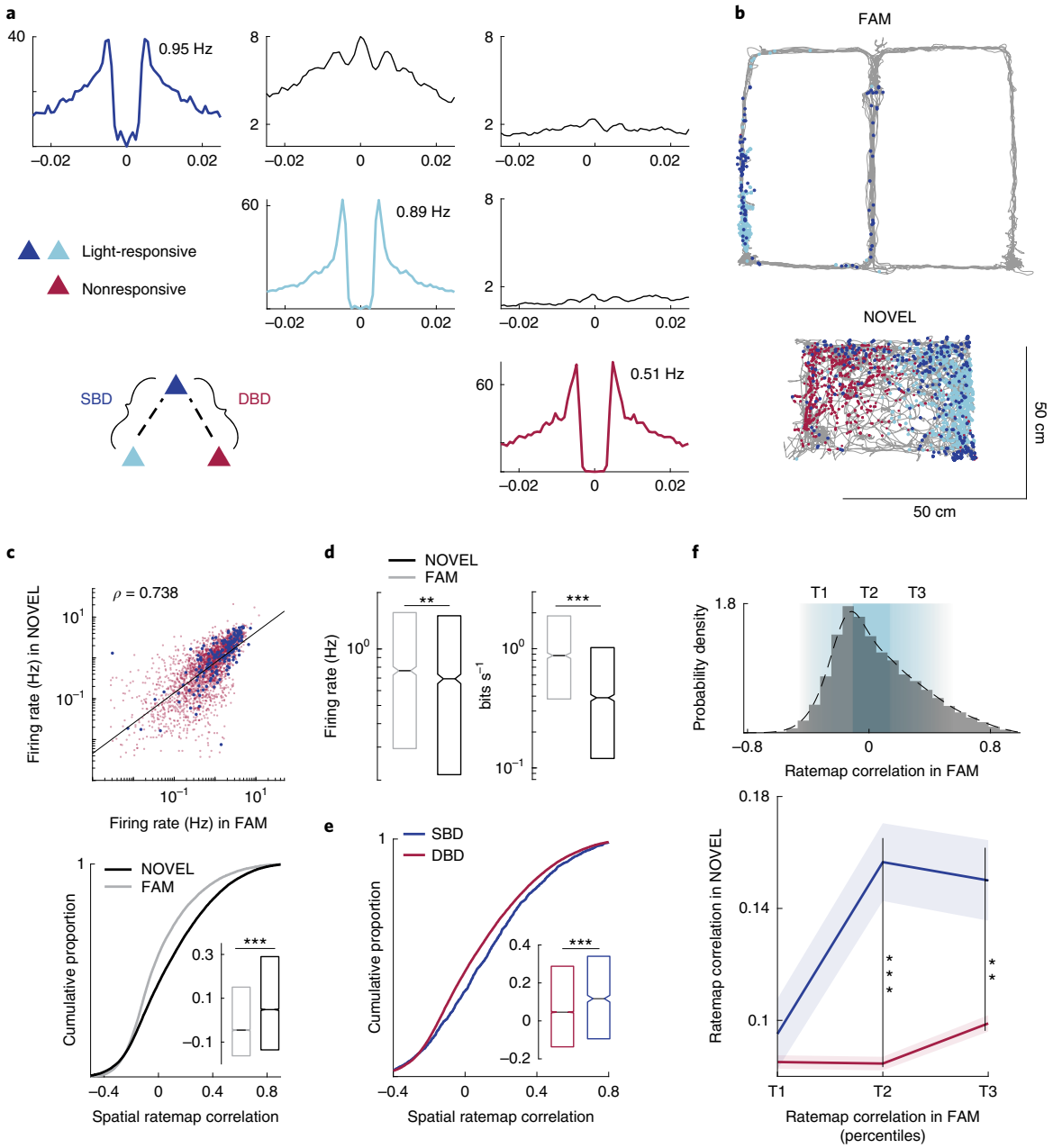

Fig. 6 | SBD neurons exhibit representational similarity across multiple novel environments. a, Autocorrelograms and CCGs of light-responsive (dark and pale blue) and nonresponsive (red) pyramidal neurons. All spikes were included, except for those emitted in periods of optogenetic stimulation. **b**, Overlap of spatial firing in familiar (FAM) and novel (NOV) environments for SBD but not DBD pairs. The example highlights the same neurons as shown in **a**. **c**, Top: theta-related firing rates (Hz) for each neuron in familiar and novel environments (Spearman's $\rho = 0.7378$, $n = 2{,}544$; $P = 0$). Light-responsive and nonresponsive neurons are highlighted in blue and red, respectively. Bottom: spatial ratemap correlations in familiar (gray, $n = 31{,}067$ pairs, median = −0.045) and novel environments (black, $n = 41{,}991$, median = 0.048; $P = 3.2 \times 10^{-283}$; two-sided Wilcoxon's test). **d**, Left: theta-related firing rates (Hz) in familiar (gray, $n = 2{,}544$ neurons, median = 0.77) and novel environments (black, $n = 2{,}544$, median = 0.69; $P = 3.3 \times 10^{-3}$; two-sided Wilcoxon's test). Right: information in bits s^{-1} in familiar (gray, $n = 2{,}544$, median = 0.88) and novel environments (black, $n = 3{,}443$, median = 0.39; $P = 8 \times 10^{-116}$; two-sided Wilcoxon's test). **e**, Spatial ratemap correlations between SBD (blue, median = 0.117; $n = 1{,}510$) and DBD (red, median = 0.046; $n = 40{,}481$) pairs ($P = 4.8 \times 10^{-9}$; two-sided Wilcoxon's test) in novel environments. **f**, Top: spatial ratemap correlation distribution in the familiar environment, divided into terciles (T1–T3); bottom: spatial ratemap correlations in the novel environment (mean ± s.e.m.) in relation to the tercile in the familiar environment for SBD (blue, $n = 2{,}404$) and DBD (red, $n = 59{,}730$) pairs. A two-way ANOVA revealed a main effect of common birthdate ($F(1,41{,}175) = 32.08$, $P = 0$), tercile ($F(2,41{,}175) = 8.34$, $P = 2 \times 10^{-4}$) and their interaction ($F(2,41{,}175) = 5.78$, $P = 3.1 \times 10^{-3}$). $^{**}P < 0.01$, $^{***}P < 0.001$. Box plot's central mark, notch and edges indicate the median, its 95% CI and the 25th/75th percentiles, respectively. See Supplementary Table 5 for P values of multiple comparisons.

Given these observations, we hypothesized that convergence of SBD pyramidal neurons on to interneurons may reflect an underlying circuit motif that promotes correlated firing across brain states. To test this prediction, we analyzed all monosynaptic connections detected between pyramidal neurons and interneurons irrespective of optogenetic labeling ($n = 31{,}932$ connections out of 184,230 possible pairs). Pairs of pyramidal cells with at least one shared postsynaptic interneuron (65.27% of all pairs) displayed a

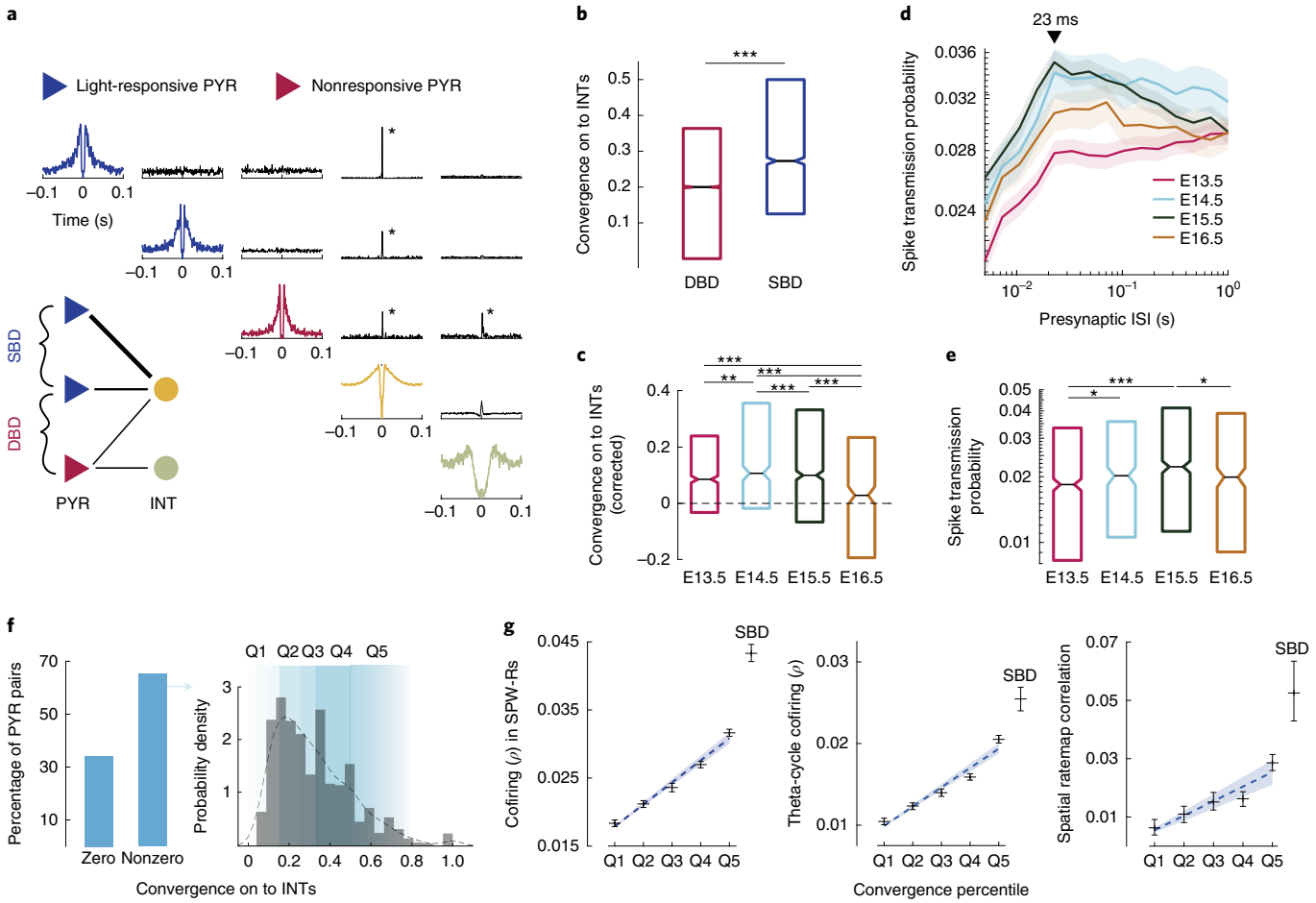

Fig. 7 | Microcircuit foundation for the correlated firing of SBD pyramidal neurons. a, Autocorrelograms of two SBD pyramidal neurons (PYR; blue: light responsive), a DBD neuron (red: nonresponsive) and their convergence on to interneurons (INTs). Sharp peaks in the CCG at 1- to 3-ms time lags revealed the presence of monosynaptic drive from pyramidal cells to interneurons[31]. Star: detected monosynaptic connection (Methods). SBD pyramidal neurons converge on to the same interneuron. **b**, Convergence on to interneurons from SBD presynaptic neuron pairs (blue, median = 0.2727; $n = 3{,}751$) and DBD pairs (red, median = 0.2; $n = 50{,}461$; $P = 2.63 \times 10^{-97}$; two-sided Wilcoxon's test). Convergence was calculated as the fraction of postsynaptic interneurons shared by a pair of presynaptic pyramidal neurons (Methods). **c**, Pyramidal cell pair convergence on to interneurons. At each birthdate, values of SBD pairs were corrected by the median convergence of DBD pairs (dashed line): E13.5, 0.0857 ($n = 1{,}200$ pairs); E14.5, 0.1071 ($n = 533$); E15.5, 0.1 ($n = 1{,}579$); E16.5, 0.0285 ($n = 439$). Medians, Kruskal–Wallis test: $H = 58.4513$, d.f. = 3, $P = 0$. **d**, Spike transmission (mean ± s.e.m.) on to postsynaptic interneurons at different presynaptic ISIs. Note the short-term depression in spike transmission probability at presynaptic ISIs of <23 ms (that is, cell assembly timescale)[32]. **e**, Spike transmission probability at 10- to 40-ms presynaptic ISIs (25–100 Hz firing), grouped by the birthdate of presynaptic pyramidal neurons: E13.5, 0.0184 ($n = 1{,}180$ pairs); E14.5, 0.0202 ($n = 440$); E15.5, 0.0222 ($n = 1{,}155$); E16.5, 0.0199 ($n = 557$). Medians, Kruskal–Wallis test: $H = 29.8231$, d.f. = 3, $P = 0$. **f**, Left: percentage of pyramidal neuron pairs with zero (34.16%, $n = 108{,}468$ pairs) and nonzero (65.27%, $n = 207{,}254$) convergence on to interneurons ($n = 96$ sessions, $n = 15$ mice). Right: convergence distribution in the nonzero subpopulation, divided into quintiles (Q1–Q5, low to high convergence). **g**, Left: cofiring in SPW-Rs across convergence quintiles. Slope of regression line = 0.0032, tStat = 13.035, $P = 1 \times 10^{-3}$ (bootstrap, two tailed). Middle: cofiring in theta cycles (slope = 0.0023, tStat = 7.15, $P = 6 \times 10^{-3}$). Right: spatial ratemap overlap (slope = 0.0049, tStat = 5.11, $P = 5 \times 10^{-3}$). Black crosses: mean ± 95% bootstrapped CI. Blue dashed line and shading: linear regression ± 95% bootstrapped CI. Correlations of SBD neurons are shown for reference. $^{*}P < 0.05$, $^{**}P < 0.01$, $^{***}P < 0.001$. Box plot's central mark, notch and edges indicate the median, its 95% CI and the 25th/75th percentiles, respectively. See Supplementary Table 4 for *P* values of multiple comparisons.

skewed convergence distribution (Fig. 7f) and all metrics of cofiring employed in the present study (cofiring in SPW-Rs, theta cycles and overlap of spatial ratemaps) exhibited a positive linear relationship with the degree of pyramidal to interneuron convergence (Fig. 7g).

Discussion

We show that sequential neurogenesis throughout embryonic development influences functional features of adult hippocampal activity patterns. Pyramidal neurons of the same birthdate exhibited strong correlations during SPW-Rs and theta waves. During behavior, SBD neurons exhibited overlapping place fields that depended on their anatomical proximity and tended to remap together across different environments. SBD neurons joined into cell assemblies, the frequency of expression of which scaled with the pool size of neurons that were born together. Our computational model suggests that pairwise correlations between SBD neurons interact with the bell-shaped wave of neurogenesis to generate diverse rates of assembly expression, as observed in our data. A potential mechanism of the similar physiological and behavioral correlations of SBD pyramidal neurons is their convergence on to the same local interneurons. Altogether, we hypothesize that a common developmental origin of hippocampal pyramidal cells biases their microcircuit arrangement, which both constrains and predicts single-neuron and population firing features in the adult brain.

Embryonic origins of the CA1 microcircuit architecture. The hippocampus can be conceived as a uniform large unit and its single-layer archicortical organization is often contrasted to the modularly organized multi-layer neocortex[1,33]. Yet, there appears to be a qualitatively similar Bauplan to the six-layer isocortex, with a gradual vertical expansion of pyramidal neurons from the hippocampus to subiculum to entorhinal cortex. From this viewpoint, the CA1 pyramidal layer may be regarded as a 'compressed' version of the six-layer neocortex, displaying radial axis differences in input–output connectivity. This hypothesis resonates with the two-sublayer distinction along the radial axis: pyramidal cells located closer to the stratum oriens (or 'deep' sublayer) and stratum radiatum (or 'superficial' sublayer) are different in size and density across a wide range of species[7,33]. Numerous recent studies have validated this approximation, based on gene expression, anatomical features, afferent/efferent connections, biophysical properties, differential pyramidal–interneuron interactions, population cooperativity and behavioral correlates[8–12,14,15].

Our birthdating observations based on in utero electroporation support and refine the deep-to-superficial organization of subcircuits within the CA1 pyramidal layer. A subset of physiological parameters we examined varied monotonically with birthdate and was largely consistent with reported differences between deep and superficial cells. Average firing rates and afferent response properties of pyramidal neurons, as reflected by their theta-phase shift during REM sleep, faithfully reflected the inside-out addition of newborn cells to the pyramidal layer (Fig. 1). However, in many measures—burstiness, SPW-R-related firing rates, theta-depth modulation and spatial information content (Figs. 1, 2 and 5)—early and late born neurons (deep and superficial, respectively) displayed quantitative similarities that could not be attributed to differences in radial position (Extended Data Fig. 3). These observations resonate with a recent report demonstrating that many biophysical and anatomical properties of ventral CA1 pyramidal neurons are better explained by birthdate than anatomical positioning[22]. A small group of earliest born (E12.5) 'pioneer' neurons exhibited unique biophysical properties and a broad dispersion in the pyramidal layer, with a tendency bias toward the stratum oriens[22]. Taken together, these findings suggest that the deep-superficial distribution is graded rather than step like, with neurons born at different time points showing broad and strongly overlapping topography (Fig. 1). As a result of the anatomical overlap between neurons of distinct birthdate, the depth criterion alone is not a robust separator of either anatomical or physiological features.

Neurons born together wire and fire together. A dominant framework portrays neural systems in which sensory inputs sculpt connectivity and dynamic patterns via activity-dependent plasticity ('neurons that fire together, wire together')[34]. In such models, there is a fundamental tension between competing features of plasticity and circuit stability, often leading to 'catastrophic interference' with previously stored knowledge[35]. Alternatively, neuronal circuits can give rise to and maintain stable preconfigured dynamics, often referred to as attractors, manifolds or neural schemata[36–38]. Such preconfigured networks internally generate and maintain a large reservoir of activity patterns available for matching with new experiences[18,39–41]. Our study was designed to examine early development as a potential source of such preconfigured dynamics[23].

The most robust finding of our experiment is a shared interrelationship of neurons born on the same day compared with neurons born on different days. Hippocampal neurons, born and developed together, innervated the same target interneurons (Fig. 7). We extended these findings to our entire database and showed that pairs of pyramidal neurons targeting the same interneurons displayed stronger cofiring statistics, much like the SBD populations. We speculate that common birthdate may be one variable responsible for setting up pyramidal-to-interneuron convergences, which motivates further scrutiny of this motif given its availability in datasets that do not involve birthdating. In a complementary fashion, other studies have shown that SBD neurons exhibit structured connectivity between subregions of the hippocampus[25], with highly clustered connectivity on to specific dendritic compartments[26]. Furthermore, CA1 pyramidal 'sister' neurons born from the same parent progenitor receive common synaptic inputs from nearby fast spiking interneurons[28].

Altogether, this wiring logic is reminiscent of microcircuits in the neocortex, where layer-specific neurons receive structured input and exhibit reciprocal connections between principal cells and interneurons[42]. Furthermore, some cortical interneuron types in superficial layers asymmetrically suppress spiking activity in deeper layers, routing firing patterns in a top-down direction[43]. In the hippocampus, deep CA1 pyramidal cells receive stronger inhibition from parvalbumin-expressing basket cells, whereas superficial pyramidal cells provide stronger excitatory inputs to basket cells. Furthermore, within the deep sublayer, parvalbumin-expressing basket cells asymmetrically inhibit pyramidal cells with different target projections[9,10], allowing selective and differential routing of CA1 outputs. Thus, the fundamental motif organization rules may be similar in the hippocampus and isocortex.

The CA1 microcircuit domains, determined by embryonic development, constrained and predicted single-neuron and population firing features in the adult brain. SBD neurons showed stronger spike correlations, firing together in the same SPW-Rs and the same theta cycles (Fig. 2). We also demonstrated that SBD pyramidal neurons exhibit overlapping spatial receptive fields and their biased place tuning persisted across the left and right arms of the figure-eight maze, and even across multiple different environments (Figs. 5 and 6). Given their recently reported overlapping efferents outside the hippocampus[22], synchronous firing of SBD pyramidal neurons can more effectively discharge their postsynaptic targets across a wider range of brain states than DBD neurons. Similar results may also hold for clonally related pairs of sister cells, which exhibit temporal cofiring in the hippocampal slice preparation[28] and are known to exhibit similar orientation tuning in the visual cortex[44,45].

These findings support the preconfigured model and are corroborated by previous observations. In intracellular studies, spatially uniform depolarization of pyramidal cells gave rise to reliable firing at a fixed spatial position[17]. Subsequent experiments used short-pulse optogenetic probing and artificial place field induction to reveal that induced fields pre-existed where place fields with suprathreshold spiking subsequently emerged, and the locations of unmasked place fields were predictable from their correlated activity with peer neurons during sleep before optogenetic unmasking[19,20]. Such pre-existing circuit constraints can explain why place cell sequences in a novel environment can be predicted from SPW-R-associated 'preplay' sequences during sleep before the experience[18,30]. In developing rats, the first exploratory trip beyond the confines of the nest takes place between postnatal days 15 and 17, and CA1 pyramidal neurons already display adult-like place fields and ordered place cell sequences on the very first exploration[46,47]. Our findings indicate that prenatal development of hippocampal circuits plays a critical role in forming a reservoir of preconfigured activity patterns that can be linked to new experiences.

In our experiments, SBD pyramidal neurons with shared spatial properties were often nearby neighbors. The existence of these functional microdomains is at variance with a strictly random organization view of spatial representation by hippocampal neurons[3], which has remained the prevailing view despite observations of anatomically clustered activity using calcium imaging[48] and, more recently, using multineuronal intracellular recordings[49]. A practical explanation of the controversy is that tetrode recordings

cannot reliably resolve place cells with overlapping place fields on the same tetrode and neighboring tetrodes are typically placed >400 µm from each other, precluding the routine detection of such domains. Furthermore, the difficulty of establishing a consensus on such peer domains might be explained by unique prenatal migration mechanisms in the hippocampus. In the neocortex, radially migrating excitatory neurons derived from the same progenitors migrate radially and organize themselves into vertical functional columns[50]. In contrast, post-mitotic hippocampal neurons use multiple radial glial fibers as scaffolds and migrate radial tangentially in a zigzag manner to establish horizontal clusters[28,51]. Consistent with this generative process, SBD pyramidal neurons expressed overlapping spatial representations at anatomical distances ≤250 µm (Fig. 5), thus revealing a developmentally established functional microtopography in the hippocampus. Intermingling of DBD neurons in the ~50-µm thin pyramidal layer may further clarify why the anatomical clustering of functional features has been hard to establish conclusively in the hippocampus. In future works, transcriptional profiling, identifying new marker genes of developmentally defined hippocampal neurons and their targeted perturbations (for example, CRISPR (clustered regularly interspaced short palindromic repeats)–Cas gene editing), will be invaluable for causally testing the behavioral functions of microdomain organization.

The wave of neurogenesis affects connectivity and activity. A number of physiological measures (that is, bursting, SPW-R-related firing, theta-depth modulation and spatial information content) displayed a U- or inverted-U-shaped relationship with birthdate. This profile reflects the known bell-shaped wave of neurogenesis[24,25], which was apparent in our data in the fractions of light-responsive pyramidal neurons observed at four distinct birthdates (Fig. 1). Perhaps most notably, the expression rate of assemblies also took on a bell-shaped profile as a function of the birthdate of assembly members (Fig. 3). Although intrinsic properties of birthdated hippocampal neurons have recently been documented[22], the consequences of the wave-like neurogenesis profile on network-wide activity have not been previously considered.

Development of large networks composed of nonidentical elements is governed by robust self-organizing phenomena that go beyond the particulars of the individual constituents. The two key features of such networks with a high degree of self-organization are growth and preferential attachment[52]. Similarly, we found that the pace of neurogenesis alone cannot explain our observations, in that the bell-shaped assembly expression rates are not a simple consequence of the bell-shaped neurogenesis wave (Fig. 4). Instead, our model suggested that, in addition to the neurogenesis wave (growth), a spike correlation rule ('attachment') must also be in place to accommodate the empirically observed assembly behavior. This additional rule might be the birth rate-dependent correlated strengthening of the reciprocal connections between SBD pyramidal cells and their interneurons[28] and/or preferred co-innervation of SBD neurons from upstream SBD peer neurons[25,26]. Our model also suggests the existence of a developmental time constant (~2 h, Fig. 4) that shapes correlated firing, although its exact value remains an empirical question.

In summary, we suggest that the radial topography and heterogeneity of functional features within the CA1 pyramidal layer results from a combination of neuronal birthdate and the rate of neurogenesis. These rules may generalize to other cortical networks.

Online content

Any methods, additional references, Nature Research reporting summaries, extended data, supplementary information, acknowledgements, peer review information; details of author contributions and competing interests; and statements of data and code availability are available at https://doi.org/10.1038/s41593-022-01138-x.

Received: 8 September 2021; Accepted: 12 July 2022;
Published online: 22 August 2022

References

1. Amaral, D., & Lavenex, P. in *The Hippocampus Book* (eds P. Andersen et al.) Hippocampal Neuroanatomy (Oxford University Press, 2007).
2. O'keefe, J. & Nadel, L. *The Hippocampus as a Cognitive Map* (Oxford Univ. Press, 1978).
3. Redish, A. D. et al. Independence of firing correlates of anatomically proximate hippocampal pyramidal cells. *J. Neurosci.* **21**, RC134–RC134 (2001).
4. Bittner, K. C. et al. Conjunctive input processing drives feature selectivity in hippocampal CA1 neurons. *Nat. Neurosci.* **18**, 1133–1142 (2015).
5. Muller, R. U., Stead, M. & Pach, J. The hippocampus as a cognitive graph. *J. Gen. Physiol.* **107**, 663–694 (1996).
6. Treves, A. & Rolls, E. T. Computational analysis of the role of the hippocampus in memory. *Hippocampus* **4**, 374–391 (1994).
7. Slomianka, L., Amrein, I., Knuesel, I., Sørensen, J. C. & Wolfer, D. P. Hippocampal pyramidal cells: the reemergence of cortical lamination. *Brain Struct. Funct.* **216**, 301–317 (2011).
8. Mizuseki, K., Diba, K., Pastalkova, E. & Buzsáki, G. Hippocampal CA1 pyramidal cells form functionally distinct sublayers. *Nat. Neurosci.* **14**, 1174–1181 (2011).
9. Lee, S.-H. et al. Parvalbumin-positive basket cells differentiate among hippocampal pyramidal cells. *Neuron* **82**, 1129–1144 (2014).
10. Valero, M. et al. Determinants of different deep and superficial CA1 pyramidal cell dynamics during sharp-wave ripples. *Nat. Neurosci.* **18**, 1281–1290 (2015).
11. Cembrowski, M. S. et al. Spatial gene-expression gradients underlie prominent heterogeneity of CA1 pyramidal neurons. *Neuron* **89**, 351–368 (2016).
12. Masurkar, A. V. et al. Medial and lateral entorhinal cortex differentially excite deep versus superficial CA1 pyramidal neurons. *Cell Rep.* **18**, 148–160 (2017).
13. Navas-Olive, A. et al. Multimodal determinants of phase-locked dynamics across deep-superficial hippocampal sublayers during theta oscillations. *Nat. Commun.* **11**, 2217 (2020).
14. Fattahi, M., Sharif, F., Geiller, T. & Royer, S. Differential representation of landmark and self-motion information along the CA1 radial axis: self-motion generated place fields shift toward landmarks during septal inactivation. *J. Neurosci.* **38**, 6766–6778 (2018).
15. Sharif, F., Tayebi, B., Buzsáki, G., Royer, S. & Fernandez-Ruiz, A. Subcircuits of deep and superficial CA1 place cells support efficient spatial coding across heterogeneous environments. *Neuron* **109**, 363–376 (2021).
16. Lee, J. S., Briguglio, J. J., Cohen, J. D., Romani, S. & Lee, A. K. The statistical structure of the hippocampal code for space as a function of time, context, and value. *Cell* **183**, 620–635 (2020).
17. Lee, D., Lin, B.-J. & Lee, A. K. Hippocampal place fields emerge upon single-cell manipulation of excitability during behavior. *Science* **337**, 849–853 (2012).
18. Dragoi, G. & Tonegawa, S. Preplay of future place cell sequences by hippocampal cellular assemblies. *Nature* **469**, 397–401 (2011).
19. McKenzie, S. et al. Preexisting hippocampal network dynamics constrain optogenetically induced place fields. *Neuron* **109**, 1040–1054 (2021).
20. Valero, M., Zutshi, I., Yoon, E. & Buzsáki, G. Probing subthreshold dynamics of hippocampal neurons by pulsed optogenetics. *Science* **375**, 570–574 (2022).
21. Villette, V., Malvache, A., Tressard, T., Dupuy, N. & Cossart, R. Internally recurring hippocampal sequences as a population template of spatiotemporal information. *Neuron* **88**, 357–366 (2015).
22. Cavalieri, D. et al. CA1 pyramidal cell diversity is rooted in the time of neurogenesis. *eLife* **10**, e69270 (2021).
23. Cossart, R. & Khazipov, R. How development sculpts hippocampal circuits and function. *Physiol. Rev.* **102**, 343–378 (2022).
24. Angevine Jr, J. B. Time of neuron origin in the hippocampal region: an autoradiographic study in the mouse. *Exp. Neurol.* Suppl. 2, 1–70 (1965).
25. Deguchi, Y., Donato, F., Galimberti, I., Cabuy, E. & Caroni, P. Temporally matched subpopulations of selectively interconnected principal neurons in the hippocampus. *Nat. Neurosci.* **14**, 495–504 (2011).
26. Druckmann, S. et al. Structured synaptic connectivity between hippocampal regions. *Neuron* **81**, 629–640 (2014).
27. Lopes-dos-Santos, V., Ribeiro, S. & Tort, A. B. Detecting cell assemblies in large neuronal populations. *J. Neurosci. Methods* **220**, 149–166 (2013).
28. Xu, H.-T. et al. Distinct lineage-dependent structural and functional organization of the hippocampus. *Cell* **157**, 1552–1564 (2014).
29. Krumin, M. & Shoham, S. Generation of spike trains with controlled auto- and cross-correlation functions. *Neural Comput.* **21**, 1642–1664 (2009).
30. Grosmark, A. D. & Buzsáki, G. Diversity in neural firing dynamics supports both rigid and learned hippocampal sequences. *Science* **351**, 1440–1443 (2016).

31. English, D. F. et al. Pyramidal cell-interneuron circuit architecture and dynamics in hippocampal networks. *Neuron* **96**, 505–520 (2017).
32. Harris, K. D., Csicsvari, J., Hirase, H., Dragoi, G. & Buzsáki, G. Organization of cell assemblies in the hippocampus. *Nature* **424**, 552–556 (2003).
33. Lorente de N¢, R. Studies on the structure of the cerebral cortex. II. Continuation of the study of the ammonic system. *J. Psychol. Neurol.* **46**, 113–177 (1934).
34. Hebb, D. O. *The Organisation of Behaviour: A Neuropsychological Theory* (Science Editions, 1949).
35. McClelland, J. L. Incorporating rapid neocortical learning of new schema-consistent information into complementary learning systems theory. *J. Exp. Psychol. Gen.* **142**, 1190 (2013).
36. Hopfield, J. J. Neural networks and physical systems with emergent collective computational abilities. *Proc. Natl Acad. Sci. USA* **79**, 2554–2558 (1982).
37. McKenzie, S. et al. Hippocampal representation of related and opposing memories develop within distinct, hierarchically organized neural schemas. *Neuron* **83**, 202–215 (2014).
38. Tse, D. et al. Schemas and memory consolidation. *Science* **316**, 76–82 (2007).
39. Edelman, G. M. Neural Darwinism: selection and reentrant signaling in higher brain function. *Neuron* **10**, 115–125 (1993).
40. Battaglia, F. P., Sutherland, G. R., Cowen, S. L., Mc Naughton, B. L. & Harris, K. D. Firing rate modulation: a simple statistical view of memory trace reactivation. *Neural Netw.* **18**, 1280–1291 (2005).
41. György Buzsáki, M. *The Brain from Inside Out* (Oxford Univ. Press, 2019).
42. Markram, H. et al. Interneurons of the neocortical inhibitory system. *Nat. Rev. Neurosci.* **5**, 793–807 (2004).
43. Yoshimura, Y. & Callaway, E. M. Fine-scale specificity of cortical networks depends on inhibitory cell type and connectivity. *Nat. Neurosci.* **8**, 1552–1559 (2005).
44. Li, Y. et al. Clonally related visual cortical neurons show similar stimulus feature selectivity. *Nature* **486**, 118–121 (2012).
45. Ohtsuki, G. et al. Similarity of visual selectivity among clonally related neurons in visual cortex. *Neuron* **75**, 65–72 (2012).
46. Farooq, U. & Dragoi, G. Emergence of preconfigured and plastic time-compressed sequences in early postnatal development. *Science* **363**, 168–173 (2019).
47. Langston, R. F. et al. Development of the spatial representation system in the rat. *Science* **328**, 1576–1580 (2010).
48. Dombeck, D. A., Harvey, C. D., Tian, L., Looger, L. L. & Tank, D. W. Functional imaging of hippocampal place cells at cellular resolution during virtual navigation. *Nat. Neurosci.* **13**, 1433–1440 (2010).
49. Noguchi, A., Huszár, R., Morikawa, S., Buzsáki, G. & Ikegaya, Y. Inhibition allocates spikes during hippocampal ripples. *Nat. Commun.* **13**, 1280 (2022).
50. Rakic, P. in *Evolutionary Developmental Biology of the Cerbral Cortex* (eds Gregory R. Bock &, Gail Cardew) 30–45 (John Wiley, 2000).
51. Kitazawa, A. et al. Hippocampal pyramidal neurons switch from a multipolar migration mode to a novel 'climbing' migration mode during development. *J. Neurosci.* **34**, 1115–1126 (2014).
52. Barabási, A.-L. & Albert, R. Emergence of scaling in random networks. *Science* **286**, 509–512 (1999).

Methods

Animals. All experiments were conducted in accordance with the Institutional Animal Care and Use Committee of New York University Medical Center (IA15-01466). Time-pregnant C57BL/6J female mice were either bred in-house or obtained from Charles River Laboratory. Timed pregnancies were prepared by co-housing males and females shortly before the dark cycle. Early morning of the next day was considered embryonic (E) age 0.5. Time-pregnant mice and their offspring were kept on a regular light:dark cycle. Electrode-implanted adult mice (3–6 months) were housed individually on a reverse light:dark cycle. At the end of all experiments, animals were deeply anesthetized with isoflurane and transcardially perfused with 4% paraformaldehyde. Brains were post-fixed in 4% paraformaldehyde for 1 d, and then moved to 1× phosphate-buffered saline (PBS). Brain slices were taken on a vibratome at 50 µm (LEICA VT10000 S).

Fluorescent microscopy. Slices were mounted on to glass slides, stained with DAPI (SouthernBiotech), and imaged under a fluorescent microscope (OLYMPUS BX61VS) with a magnification of ×10 under three filters: DAPI, tetramethylrhodamine (TRITC; for tdTomato) and FITC (for eYFP). This procedure was followed to verify the presence of electroporated plasmids and to analyze the somatic radial position (see below).

Quantification of normalized cell depth. CA1 pyramidal neuron coordinates were identified by thresholding expression in the red spectrum (tdTomato), followed by manual curation (ImageJ). In each section, the CA1 region was delimited according to the Mouse Brain Atlas[53]. The border between stratum pyramidale (SP) and stratum radiatum (SR), as well as the border between SP and stratum oriens (SO), were identified manually assisted by the high contrast of DAPI expression (Extended Data Fig. 1). Using customized written scripts, a perpendicular projection was made from each identified pyramidal neuron to the SP–SR border. Connecting the cell and its projection foot on the SP–SR border, an extension was made to cross the SP–SO border. This distance was taken to be the local thickness of the pyramidal layer. The perpendicular distance from each neuron to its projection on to the SP–SR border was divided by the local layer thickness to obtain the neuron's normalized depth[54] ($n=3$ E13.5 brains, $n=4$ E14.5 brains, $n=3$ E15.5 brains and $n=4$ E16.5 brains were used for this quantification).

In utero hippocampal electroporation. Birthdating of CA1 pyramidal neurons was performed via in utero electroporation[55] in embryos of time-pregnant females at E13.5 ($n=26$ mothers, ~7% successful), E14.5 ($n=4$, ~50% successful), E15.5 ($n=13$, ~70% successful) and E16.5 ($n=4$, 100% successful). Success rate refers to the fraction of litters in which at least one offspring survived and expressed the electroporated DNA constructs. All surgeries were performed in the morning. Time-pregnant female mice were anesthetized with isoflurane (1.5–2% isoflurane at 1 l min^{-1} air-flow rate) with vital signs monitored throughout the procedure. A subcutaneous injection of 5 mg kg^{-1} of meloxicam was delivered for analgesia. The central portion of the uterine horn was extracted and placed on sterile gauze humidified with PBS. Using a pulled glass capillary, a plasmid DNA solution mixed with Fast Green FCF dye (Fisher) was injected (Picospritzer II, Parker) into the lateral ventricles of each embryo. The DNA solution consisted of ChR2-eYFP at 1.2 µg µl^{-1} (pAAV-CaMKIIa-hChR2(H134R)-EYFP; Addgene plasmid no. 26969; http://n2t.net/addgene:26969; RRID: Addgene_26969) and pCAG-tdTomato at 0.65 µg µl^{-1} (Addgene plasmid no. 83029; http://n2t.net/addgene:83029; RRID: Addgene_83029). Plasmids and Fast Green were diluted in sterile 1× PBS. After injection, plasmids were electroporated toward the progenitors of CA1 pyramidal neurons using the triple electrode technique (CUY700 and CUY650 electrode series from Nepagene) (Fig. 1a)[55]. Electroporation involved five 50-ms pulses at 35–45 V (depending on the age of embryos), with 500-ms interpulse intervals (ECM 830, Harvard Apparatus). As the locus of targeted pyramidal neurogenesis (ventricular zone) occurs far away from the locus of interneuron neurogenesis (ganglionic eminences), the probability of off-target expression in interneurons is very low. After the procedure, the uterine horn was placed back in the abdomen, and the anterior muscle wall and overlying skin were sutured. After birth, dams were cohoused with the pups until these had reached weaning age (3–4 weeks). At that point, the male and female pups were housed separately.

Subsequent data collection and analysis were not performed blind to the in utero electroporation conditions. Animals were allocated to groups based on the embryonic age when in utero electroporation occurred (E13.5, E14.5, E15.5 or E16.5), so randomization was not part of the experimental design. No statistical methods were used to predetermine group sizes, which were designed to be similar to those reported in previous publications[30].

BrdU experiments. Using in utero electroporation to measure the rate of neurogenesis (as is stated in the main text) might be confounded by many factors, such as the anatomy of the embryo, efficiency of pulsing and the surface area of the electrode. Yet, previous studies that used BrdU labeling of dividing cells in the hippocampal CA1 and CA3 regions reported a bell-shaped wave of neurogenesis[25], which was consistent with previous studies using autoradiography[24]. We observed a similarly shaped distribution using in utero electroporation (Fig. 1e).

Other experiments have shown that DNA electroporated toward cortical progenitors is taken up by dividing cells most effectively when these are in the phase of the cell cycle (S–G2) associated with the most effective incorporation of BrdU[56]. We extended these findings to hippocampal neurons by combining in utero electroporation with simultaneous intraperitoneal infusion of BrdU[51]. We followed a previous protocol to calibrate the use of replication-deficient adeno-associated viruses for birthdating neurons in the entorhinal cortex[57]. Briefly, time-pregnant female mice (E14.5–E15.5) that underwent in utero electroporation of CAG-tdTomato (described above) were given a single intraperitoneal injection of BrdU (Thermo Fisher Scientific, catalog no. B23151; 40 mg kg^{-1}) at various time lags with respect to electroporation. Pups were sacrificed between postnatal days 7 and 10, brains were fixed overnight in 4% paraformaldehyde and sectioned coronally at 50-µm thickness. To stain against BrdU and tdTomato, sections were boiled at 90 °C in 10 mM citric sulfate, pH 6.0 to expose nuclear epitopes and then underwent four 10-min washes in 1× PBS before a 2-h blocking stage (10% goat serum, 0.2% bovine serum albumin and 0.05% Triton-X in 1× PBS). Primary antibodies against BrdU (1:250; OriGene, catalog no. TA190126) and red fluorescent protein (1:500; Rockland, catalog no. 600-401-379) were incubated overnight at room temperature in a carrier solution comprising 1% goat serum, 0.2% bovine serum albumin and 0.05% Triton-X in 1× PBS. After four 10-min washes in 1× PBS, slices were incubated for 2 h at room temperature with the following secondary antibodies in carrier solution: anti-rat Alexa Fluor-647 (1:500; Thermo Fisher Scientific, catalog no. A-21247) and anti-rabbit Alexa Fluor-488 (1:500; Thermo Fisher Scientific, catalog no. A-11008).

Images were collected with a Zeiss LSM 800 using a ×20 Plan-Apochromat,×20 numerical aperture, 0.8 lens and pinhole set to 1–1.18 Airy units. The z series were collected over 15 µm at 1-µm steps.

Analysis was performed using a semi-automated pipeline in ImageJ. Briefly, manually drawn regions of interest (ROIs) of tdTomato$^+$ neurons were associated with the z plane where they exhibited maximum fluorescence intensity. The ROI-associated mean intensity of the BrdU signal was thresholded to identify double-labeled neurons. Thresholds were determined for each z series based on the distribution of pixel intensities in the pyramidal layer (2 s.d. above mean).

Silicon probes coupled with optic fibers for optogenetics. High-density silicon probes were mounted on fully recoverable and reusable three-dimensional (3D) printed micro drives[58]. Silicon probes used in the present study were the following: ASSY-156-E-1 (Cambridge NeuroTech), ASSY Int128-P64-1D (Diagnostic Biochips) and ASSY Int64-P32-1D (Diagnostic Biochips). The last two types were dual-sided designs, equipped with recording sites on both sides of each shank. The spacing between shanks was 250 µm. Once mounted on a microdrive, probes were coupled with a single 100-µm diameter optic fiber with a ferrule attached to one of its ends (Thor labs). Blue light (450 nm) was delivered via laser diodes (catalog no. PL450B, Arrow Inc.) and controlled by the open-source Cyclops LED driver (https://github.com/jonnew/cyclops)[59]. Before coupling with the probe and implantation, optic fiber quality was assessed by measuring the maximum light intensity (catalog no. PM100D, Thor labs) at the fiber tip. A maximum output of at least 8 mW mm^{-2} was required.

Implantation and recording. Chronic recordings were performed from $n=17$ freely moving adult mice (12 males, 5 females; age 3–6 months; electroporated at: E13.5, $n=4$; E14.5, $n=3$; E15.5, $n=6$; E16.5, $n=4$) for ~4–12 weeks (Supplementary Table 1). The mice were anesthetized with 1.5–2% isoflurane and implanted with silicon probes coupled with optic fibers directed at the dorsal CA1 region. A stainless-steel screw was placed over the cerebellum for grounding and reference, and a craniotomy was drilled at −2 mm anteroposterior (AP) and 1.7 mm mediolateral. An acute probe equipped with an optic fiber was slowly lowered above the hippocampus (~600–1,000 µm) and square light pulses (100 ms) were delivered to verify ChR2 expression. If reliable optical responses were not observed in either hemisphere, surgery was terminated and the animal was euthanized with an overdose of isoflurane. Otherwise, a silicon probe/optic fiber attached to a 3D printed microdrive was implanted at a 45° angle with respect to the AP axis at a depth of approximately 700 µm. Due to lateralization of electroporated ChR2, approximately half the animals were implanted in their left hemisphere and the remaining half in their right. Craniotomies were sealed with a mix of dental wax and mineral oil, and a copper mesh cage was constructed to provide electrical and mechanical shielding. Postoperatively, animals received a single intramuscular injection of 0.06 mg kg^{-1} of buprenorphine (0.015 mg ml^{-1}) and as needed for the next 1–3 d. Animals were allowed a 7-d recovery period before the start of experiments.

After a 7-d recovery period, neural signals were recorded in the homecage while probes were lowered into the CA1 pyramidal layer, which was identified physiologically via the sharp wave polarity reversal. Neural data were amplified and digitized at 30 kHz using Intan amplifier boards (catalog no. RHD2132/RHD2000, Evaluation System). All recordings (92 sessions ranging in duration from 113.7 min to 475.6 min; median duration = 309.1 min) included a homecage period of sleep and wake.

See Supplementary Table 1 for an overview of which animals were employed for analyses described in the main text. Two E13.5 animals were excluded for analyses in Extended Data Fig. 4 due to a lack of SBD pairs.

Behavior. A subset of $n=9$ mice (E13.5, $n=2$; E14.5, $n=2$; E15.5, $n=2$; E16.5, $n=3$) was trained on a spatial alternation task in a figure-eight maze (Supplementary Table 1). Animals were water restricted before the start of experiments and familiarized to a customized 79×79 cm^2 figure-eight maze (Fig. 5a) raised 61 cm above the ground[60]. Over several days after the start of water deprivation, animals were shaped to visit alternate arms between trials to receive a water reward in the first corner reached after making a correct left/right turn. A 5-s delay in the start area was introduced between trials. The length of each trial was 205 cm. Infrared (IR) sensors were used to detect the animal's progression through the task and 3D printed doors mounted to servo motors were opened/closed to prevent the mice from backtracking (Fig. 5a). IR sensors and servo motors were controlled by a customized Arduino-based circuit[60]. The position of head-mounted red LEDs (light-emitting diodes) was tracked with an overhead Basler camera (catalog no. acA1300-60 gmNIR, Graftek Imaging) at a frame rate of 30 Hz, and tracking data were aligned to the recording via transistor–transistor logic pulses from the camera, as well as a slow pulsing LED located outside the maze. Animals were required to run at least ten trials along each arm (at least twenty trials total) within each session. In all sessions that included behavior, animals spent ~120 min in the homecage before running on the maze and another ~120 min in the homecage afterward. All behavioral sessions were performed in the mornings (start of the dark cycle).

To explore the reorganization of place tuning across different environments, a subset of $n=3$ mice (Supplementary Table 1) that underwent in utero electroporation was exposed to novel environments in addition to the familiar figure-eight maze. After the shaping phase described above, animals underwent recording sessions consisting of a ~120-min homecage period, running on the figure-eight maze, ~60-min homecage period, running in a never-before experienced environment, followed by a final ~120-min homecage period (Fig. 6). In some sessions, animals were exposed to two distinct novel environments, with a ~60-min homecage period in between. Altogether, we obtained $n=16$ novel environment explorations across animals. Six distinct novel environments were employed: two linear tracks, three open fields and one figure-eight maze. Mazes were placed in distinct recording rooms, or in different corners of the same recording room, with distinct enclosures to ensure unique visual cues. Animal tracking was performed as described above.

Stimulation protocol. Square light pulses in blocks of five with increasing light intensity and 200-ms interpulse intervals were delivered to induce spiking in ChR2-expressing, birthdated pyramidal neurons. Pulse duration was fixed within each session but varied across (range 1.5–3 ms; median = 2 ms within session). A range of 300–1,600 blocks per session was delivered (median = 800 blocks per session). Optogenetic stimulation was delivered at the end of each session after the recordings were completed, while the animal rested in its homecage. Before each recording session, light intensities were calibrated to a level with observable spiking, but no local field potential (LFP) deflection that would reflect a population effect (Extended Data Fig. 1). Sharp onsets and offsets were associated with a photoelectric artifact that took the form of a spikelet. To prevent such artifacts from propagating to spike sorting and unit identification, raw data were clipped out in the interval shortly before the onset (0.15 ms) and after the offset (0.8 ms) of each brief pulse.

Unit isolation and classification. Spikes were extracted and classified into putative single units using KiloSort1 (ref. [61]). Manual curation was performed in the Phy2 software with the aid of customized plugins (https://github.com/petersenpeter/phy2-plugins). Throughout the manual curation step, isolation quality was judged by inspecting crosscorrelograms (CCGs) for incorrect splits of single units (that is, autocorrelogram structure detectable in the CCG). Cells were classified as putative pyramidal cells and interneurons via CellExplorer (https://cellexplorer.org/pipeline/cell-type-classification)[62]. Briefly, putative interneurons were identified via hard thresholds imposed on the waveform shape (trough-to-peak) and the autocorrelogram rise and decay time constants. The dataset includes a total of 7,411 well-isolated putative pyramidal cells and 2,060 putative interneurons (1,556 narrow waveform, 504 wide waveform; Extended Data Fig. 2). Cluster isolation quality was assessed using the L-ratio metric[63].

State scoring. State scoring was performed as described previously (https://github.com/buzsakilab/buzcode/blob/dev/detectors/detectStates/SleepScoreMaster/SleepScoreMaster.m)[64]. First, the LFP was extracted from wideband data by low-pass filtering (sinc filter with a 450-Hz cut-off band) and downsampling to 1,250 Hz. Three signals were used for state scoring: broadband LFP, narrowband theta frequency LFP and electromyogram (EMG). Spectrograms were computed from broadband LFP with fast-Fourier transform in 10-s sliding windows (at 1 s) and principal component analysis (PCA) was computed after a z transform. The first PC reflected power in the low (<20-Hz) frequency range, with oppositely weighted power at higher (>32-Hz) frequencies. Theta dominance was quantified as the ratio of powers in the 5- to 10-Hz and 2- to 16-Hz frequency bands. EMG was estimated as the zero-lag correlation between 300- and 600-Hz-filtered signals across recording sites. Soft sticky thresholds on these metrics were used to identify states. Briefly, high LFP PC1 and low EMG were taken to be NREM, high theta and low EMG were considered to be REM and the remaining data were taken to reflect the waking state. All assignments were inspected visually and manually curated wherever appropriate (https://github.com/buzsakilab/buzcode/blob/dev/GUITools/TheStateEditor/TheStateEditor.m).

SPW-R detection. SPW-Rs were detected as described previously[65] from manually selected channels located in the center of the CA1 pyramidal layer (https://github.com/buzsakilab/buzcode/blob/master/detectors/detectEvents/bz_FindRipples.m). Broadband LFP was bandpass filtered between 130 and 200 Hz using a fourth-order Chebyshev filter, and the normalized squared signal was calculated. SPW-R maxima were detected by thresholding the normalized squared signal at 5 s.d. above the mean, and the surrounding SPW-R start–stop times were identified as crossings of 2 s.d. around this peak. SPW-R duration limits were set to be between 20 and 200 ms. An exclusion criterion was provided by designating a 'noise' channel (no detectable SPW-Rs in the LFP) and events detected on this channel were interpreted as false positives (for example, EMG artifacts).

Detection of light-responsive, birthdated pyramidal neurons. ChR2-expressing neurons have been shown to fire at characteristic latencies with respect to stimulus onset[66–69]. However, as this may also be true of some non-ChR2-expressing neurons due to polysynaptic effects (for example, precisely timed rebound from inhibition), we additionally tested the reliability of firing after stimulus onset as opposed to preceding it. As interneurons were expected to respond due to strong convergent inputs from their presynaptic pyramidal neurons[31], only pyramidal neurons identified via unit classification were tested for light responsiveness.

The latency to spike effect was quantified using SALT[70]. For each pyramidal neuron, the distribution of latencies to first spike in 10-ms windows after each pulse was compared with independent 'baseline' latency to spike distributions ($n=200$) with respect to random timepoints outside of optogenetic stimulation. To avoid the effect of slowly changing firing rates on spike latencies, the random timepoints were selected in a period before the first pulse onset in an interval of equal duration to that between the first and last pulse. A P value was obtained by comparing the median distance (Jensen–Shannon divergence) between the post-stimulus and baseline distributions against a null computed from distances between baseline distributions. $P \leq 0.001$ was considered to be significant.

To test the reliability of poststimulus firing, we adapted a routine for the detection of monosynaptic connections[31,71]. As described previously, we computed the peristimulus time histogram (PSTH, 1-ms bins) and smoothed with a hollowed Gaussian (15 ms s.d.) to obtain a baseline estimate of peristimulus firing matched for slow changes in firing rate. We considered spike counts in 3× bins surrounding that of peak poststimulus firing and assessed whether any of these were significantly greater than baseline counts, assuming a Poisson distribution over counts at each bin. Furthermore, the bin of maximum poststimulus firing was compared with bins at similar lags preceding pulse onset, to test whether peak firing after the stimulus was significantly greater than firing preceding the stimulus. In each case, α was set at 0.001 and Bonferroni corrected for multiple comparisons.

All the above-described tests needed to be passed for a pyramidal neuron to be considered light-responsive.

Monosynaptic connection analyses. CCGs between pairs of neurons were constructed (0.8-ms bins) from spikes occurring outside optogenetic stimulation. Statistical detection of monosynaptic connections was identical to the reliability test described above for detecting light-responsive neurons. For full details of the algorithm, see English et al.[31]. Only connections from pyramidal neurons to interneurons were considered for further analysis.

To assess the effective strength of synaptic coupling at different presynaptic firing rates, the spike transmission probability metric was computed. First, CCGs were constructed from subsets of pyramidal spikes with preceding ISIs falling within a specific range[31]. The resulting CCG spike counts were divided by the number of presynaptic spikes in the subset to obtain the probability of interneuron firing at various lags with respect to the presynaptic spike. Values at 0.8- to 2.8-ms lags that exceeded the baseline probability of postsynaptic firing (obtained by convolving CCGs with an 8-ms s.d.-hollowed Gaussian) were integrated, resulting in spike transmission probability.

Convergence on to interneurons was assessed for pairs of pyramidal neurons. For each pair, the number of interneurons they both projected to (that is, convergence) was divided by the number of interneurons they targeted collectively, resulting in a convergence index that took on values between 0 and 1.

Cofiring analysis. The spike count in each interval (either a SPW-R or a theta cycle) was computed, resulting in a vector of spike counts for each pyramidal neuron. Pearson's correlation coefficients between spike count vectors of different neurons were computed to estimate the SPW-R- and theta-cycle-related cofiring of each pair.

SBD versus DBD pairs. All unique pairs of light-responsive pyramidal neurons in a given recording session were considered to be SBD. This group was compared with one comprising all unique pairs in which one pyramidal neuron was light

responsive and the other was not. These pairs were considered to be DBD. It is possible that some nonresponsive neurons failed to be targeted by in utero electroporation, and therefore a fraction of our 'DBD group' could contain some SBD pairs. However, we assumed that this fraction would be sufficiently small given the number of true DBD neurons and continued to use the term 'DBD' for convenience.

Theta-cycle detection. As theta-phase shifts along the radial axis[72], a channel with a positive sharp wave (that is, above the center of the pyramidal layer) was selected to ensure consistency of extracted phases across recordings. Broadband LFP was bandpass filtered between 6 and 12 Hz using a fourth-order Chebyshev filter. The Hilbert transform of the filtered signal was computed, and its absolute value and angle at each timepoint were taken to be the theta-band amplitude and phase, respectively. Intervals with theta-band amplitude 1 s.d. above the mean were considered for theta cycle detection. Within these intervals, timepoints where the phase crossed 0° were identified as peaks of theta, and timepoints of consecutive theta peaks were considered the onsets and offsets of individual theta cycles (all throughout, peaks are at 0° and 360° and troughs at 180°). Only theta cycles occurring within identified waking periods (see section State scoring) were considered for analysis.

REM shifting and theta-depth modulation. Theta phase was extracted in the waking and REM periods identified via state scoring. Broadband LFP was filtered and Hilbert transformed to extract amplitude and phase, as described above. In the waking state, intervals with theta-band amplitude above the mean were considered, whereas REM periods were considered in their entirety, because high theta amplitude was required for their detection in the first place. Each spike time falling within these periods was assigned a theta phase, resulting in a separate phase distribution in wake and REM. Phase locking was tested in each distribution (Rayleigh's test) and, when significant ($P<0.01$), the mean direction and mean resultant length of the circular phase distribution were taken as the preferred theta-phase and theta-depth modulation, respectively. Pyramidal neurons that were significantly phase locked in wake and REM were designated as REM shifting if their preferred phase was between 120° and 300° during wake and outside this interval during REM[8].

ICA assembly analysis. To detect assemblies reflecting higher-order coactivity among pyramidal neurons, we performed ICA as has been described previously[27,73,74]. Spikes from pyramidal neurons recorded in the homecage were binned at 1-ms resolution, smoothed with a Gaussian (25-ms full-width at half-maximum (FWHM)), and the resulting timeseries was z-scored. The number of assemblies was based on the N principal components with variances that exceeded an analytical threshold based on the Marcenko–Pastur distribution describing variances expected for uncorrelated data. The z-scored matrix was projected into the subspace spanned by these N components and ICA was performed to extract assemblies (each corresponds to an IC). As both the scale and the sign of IC weights are arbitrary, IC weights were rescaled to unit norm and multiplied by the sign of the highest absolute value weight. Pyramidal neurons with IC weights that exceeded 2 s.d. above the mean weight were considered to be 'assembly members' and all other neurons as 'assembly nonmembers'. Only assemblies with at least one light-responsive (that is, birthdated) assembly member were considered for further analysis (Fig. 3). In a separate set of analyses, weights were hardcoded to reflect assembly members made exclusively of light-responsive neurons (Extended Data Fig. 7)

The expression strength of each assembly was computed as:

$$A(t) = \boldsymbol{z}(t)^T P_i(t) \boldsymbol{z}(t) \quad (1)$$

where $P_i(t)$is the projection matrix (outer product, diagonal set to zero) of the ith IC. $A(t)$ quantifies the moment-to-moment assembly expression strength as the similarity between an IC and the instantaneous, z-scored firing pattern recorded across recorded pyramidal neurons (that is, a projected z-score). Significant peaks exceeding 2 s.d. above the mean expression strength were taken as timepoints of assembly expression, which were used for subsequent analysis (for example, assembly expression rates in SPW-Rs).

For the state-dependent assembly analyses in Extended Data Fig. 6, spikes were binned at 25-ms resolution and z-scored. For analyses in Extended Data Fig. 6a–c, SPW-Rs were binned and then concatenated to exclude correlation patterns in other brain states. Similarly, in Extended Data Fig. 6d–h, only spikes occurring on the familiar figure-eight maze were considered. To detect assemblies associated with each held-out, birthdated pyramidal neuron, we identified bins that contained its spikes and performed ICA on the submatrix of remaining pyramidal neurons. To quantify the time-resolved expression of extracted assemblies, ICs were projected on a matrix that was binned finely (1 ms) and smoothed (25 ms FWHM Gaussian) before z-scoring. In this case, all bins of the z-scored spike matrix were used. Timepoints of assembly expression and identities of assembly members were extracted as described above.

Linear–nonlinear Poisson model for exploring assembly dynamics. At least two accounts could explain the qualitative similarity between assembly expression rates (Fig. 3e) and the bell-shaped fraction of neurons labeled at each birthdate (Fig. 1e). One explanation may be based on the observation that firing rates and participation in SPW-Rs also exhibited a bell-shaped relationship with birthdate. Differences in SPW-R-related firing across birthdates may bias correlations, which may affect SPW-R-related expression rates of the detected assemblies. An alternative explanation is that SBD neurons exhibit pairwise correlations over and above those expected from the observed firing rate differences. These excess correlations may then interact with the bell-shaped rate of neurogenesis to produce differences in assembly expression rates. To explore these two accounts, we generated spike trains with controlled firing rates and pairwise correlations (Extended Data Fig. 8)[29] and compared their assembly expression rates to those observed in the data.

We relied on a nonlinear transformation of multivariate Gaussian random variables to generate non-negative stochastic processes with controlled mean and covariance:

$$x \sim \mathcal{N}(0, I) \quad (2)$$

$$\boldsymbol{\lambda} = \exp(\boldsymbol{\mu} + Lx) \quad (3)$$

where L is a lower triangular matrix, such that $\Sigma = LL^T$ and $\boldsymbol{\mu}$ are the predefined covariance and mean of a Gaussian. An exponential transformation of samples from such a Gaussian results in a non-negative, log normally distributed multivariate process $\boldsymbol{\lambda}$, with the following mean and covariance:

$$E(\boldsymbol{\lambda}) = \exp(\boldsymbol{\mu} + 0.5\mathrm{diag}(\Sigma)) \quad (4)$$

$$\mathrm{Cov}(\lambda_i, \lambda_j) = E(\lambda_i) E(\lambda_j) \left(\exp\left(\sigma^2_{i,j}\right) - 1\right) \quad (5)$$

where diag(Σ) is a vector holding the Gaussian variances and $\sigma^2_{i,j}$ the Gaussian covariance. Each λ_i can be interpreted as the time-varying firing rate of a neuron. By controlling the Gaussian variances diag(Σ) and means $\boldsymbol{\mu}$, we controlled both the firing rates λ_i and their covariances Cov(λ_i, λ_j). Furthermore, covariance Cov(λ_i, λ_j) depended on $\sigma^2_{i,j}$, which can be interpreted as an additional source of covariation that interacts with the joint firing rates of the individual neurons. Covariance Σ was generated using a squared exponential kernel:[75]

$$k_{se}(\mathrm{dob}_{\mathrm{diff}}) = \sigma^2_{\max} \exp\left(-\frac{(\mathrm{dob}_{\mathrm{diff}})^2}{2\tau^2}\right) \quad (6)$$

where $\mathrm{dob}_{\mathrm{diff}}$ refers to the difference of birthdates between two neurons. Maximum Gaussian covariance $\sigma^2_{\max}$ is achieved when $\mathrm{dob}_{\mathrm{diff}}$ is zero and decays at a timescale τ as $|\mathrm{dob}_{\mathrm{diff}}|$ increases. This kernel function captures the notion that neurons born close together in time exhibited higher covariation in their firing.

In the 'bell-shaped' model, the rate of neurogenesis was modeled as a Gaussian with mean 14.5 (denoting embryonic age) and s.d. of 1 d (Fig. 4 and Extended Data Fig. 8). In the 'uniform' model, the rate of neurogenesis was modeled as constant across birthdates (Extended Data Fig. 9). Each simulation began by drawing $n=350$ units with birthdates set according to this distribution. Gaussian covariance Σ was specified following equation (6) and equation (4) was solved for $\boldsymbol{\mu}$, which was set to ensure that average firing rates $E(\lambda_i)$ followed those empirically observed in SPW-Rs (Fig. 2f). Specifically, firing rates of units <E14 were sampled from the E13.5 firing rate distribution, units ≥E14 and ≤E15 were drawn from the E14.5 distribution, units ≥E15 and ≤E16 from the E15.5 distribution, and units >E16 from the E16.5 distribution. Samples were generated according to equations (2) and (3) to generate non-negative rate functions λ_i, and spike counts were simulated from the corresponding inhomogeneous Poisson processes. Each time step was assumed to be 25 ms and 10,000 samples (250 s) were generated per simulation.

The resulting spike matrix was z-scored, and assemblies were detected and tracked using ICA as described above. For a given set of parameters, simulations were run until $n=200$ assemblies were extracted. As each simulated neuron had a prespecified birthdate, the birthdate associated with each assembly was the average across assembly members (IC weights >2 s.d. above the mean). To compare the birthdate-dependent profile of simulated assembly expressions to data, simulated expression rates were z-scored and the average across empirically observed assembly rates was added to each value. The shape of simulated assembly expressions as a function of birthdate was captured by fitting a Gaussian process, nonlinear regression model (http://www.gaussianprocess.org/gpml/code/matlab/doc)[75], and the −log(predictive probability) under this model was computed for the observed average assembly expression rate at each birthdate. The cumulative −log(P) was considered as the error.

Simulations were performed for a range of Gaussian covariances $\sigma^2_{\max}$ and decay timescales τ to test the influence of firing rate differences (small $\sigma^2_{\max}$) and the influence of additional correlations (large $\sigma^2_{\max}$) on the organization of assemblies. For each set of parameters, we performed $n=100$ independent simulations from the uniform model and treated the resulting distribution of log(predictive probabilities) as a null for the log predictive probability achieved under the bell-shaped model, which identified regions of the parameter space where the bell-shaped model achieved a significantly better fit (Extended Data Fig. 9).

The simulation results in Fig. 4d were robust to the choice of above-described free parameters.

Spatial ratemap analyses. Trials in the figure-eight and linear mazes were linearized and velocity in each trial was estimated with a Kalman filter. Considering moments with speed >1.5 cm s^{-1}, the number of spikes and time spent in each 1-cm bin was computed separately for left and right trials and smoothed with a 9-cm FWHM Gaussian. For open field mazes, spikes and time spent were computed in bins of 1 cm × 1 cm and smoothed with a 4.5-cm FWHM Gaussian. The average ratemaps for left and right trials were computed as the smoothed spike counts normalized by the smoothed occupancy. Never-visited bins were excluded from analysis.

For spatial ratemap correlation between pyramidal neurons, ratemaps for left and right trials were concatenated and Pearson's correlation coefficient was computed. In the case of figure-eight mazes, the central stem portion (common between left and right trials) was excluded for the purpose of this analysis. In the case of open field mazes, two-dimensional spatial ratemaps were vectorized to computing ratemap correlations. Spatial information in bits s^{-1} was computed as described previously[76].

Statistical analysis. Statistical tests involving multiple group comparison (that is, analysis of variance (ANOVA) and Kruskal–Wallis test) were performed nonparametrically with bootstrap resampling to generate null distributions of the relevant test statistic (that is, F and H statistics, respectively). Specifically, datapoints across groups were pooled and reassigned to groups randomly with replacement. $N = 5{,}000$ resamplings were performed to generate the null distributions. The same was performed for the q statistic for Tukey's post-hoc comparison between groups. All post-hoc comparisons were two tailed. Group comparison was performed using a nonparametric Wilcoxon's rank-sum test, reflecting the highly skewed nature of cell metrics[77].

All ANOVAs were one way, unless noted otherwise.

Reporting summary. Further information on research design is available in the Nature Research Reporting Summary linked to this article.

Data availability

The dataset generated for the present study has been made publicly available in the Buzsáki lab repository (https://buzsakilab.nyumc.org/datasets).

Code availability

Customized MATLAB scripts are available at https://github.com/buzsakilab/buzcode and https://github.com/rhuszar.

References

53. Paxinos, G. & Franklin, K. B. *Paxinos and Franklin's The Mouse Brain in Stereotaxic Coordinates* 5th edn (Academic Press, 2019).
54. Save, L., Baude, A. & Cossart, R. Temporal embryonic origin critically determines cellular physiology in the dentate gyrus. *Cereb. Cortex* **29**, 2639–2652 (2019).
55. Dal Maschio, M. et al. High-performance and site-directed in utero electroporation by a triple-electrode probe. *Nat. Commun.* **3**, 960 (2012).
56. Stancik, E. K., Navarro-Quiroga, I., Sellke, R. & Haydar, T. F. Heterogeneity in ventricular zone neural precursors contributes to neuronal fate diversity in the postnatal neocortex. *J. Neurosci.* **30**, 7028–7036 (2010).
57. Donato, F., Jacobsen, R. I., Moser, M.-B. & Moser, E. I. Stellate cells drive maturation of the entorhinal-hippocampal circuit. *Science* **355**, eaai8178 (2017).
58. Vöröslakos, M., Petersen, P. C., Vöröslakos, B. & Buzsáki, G. Metal microdrive and head cap system for silicon probe recovery in freely moving rodent. *eLife* **10**, e65859 (2021).
59. Newman, J. P. et al. Optogenetic feedback control of neural activity. *eLife* **4**, e07192 (2015).
60. Valero, M. et al. Sleep down state-active ID2/Nkx2. 1 interneurons in the neocortex. *Nat. Neurosci.* **24**, 401–411 (2021).
61. Pachitariu, M., Steinmetz, N. A., Kadir, S. N., Carandini, M. & Harris, K. D. Fast and accurate spike sorting of high-channel count probes with KiloSort. *Adv. Neural Inf. Process. Syst.* **29**, 4448–4456 (2016).
62. Petersen, P. C., Siegle, J. H., Steinmetz, N. A., Mahallati, S. & Buzs ki, G. CellExplorer: A framework for visualizing and characterizing single neurons. *Neuron* **109**, 3594–3608 (2021).
63. Schmitzer-Torbert, N., Jackson, J., Henze, D., Harris, K. & Redish, A. Quantitative measures of cluster quality for use in extracellular recordings. *Neuroscience* **131**, 1–11 (2005).
64. Levenstein, D., Buzsáki, G. & Rinzel, J. NREM sleep in the rodent neocortex and hippocampus reflects excitable dynamics. *Nat. Commun.* **10**, 2478 (2019).
65. Tingley, D. & Buzsáki, G. Routing of hippocampal ripples to subcortical structures via the lateral septum. *Neuron* **105**, 138–149 (2020).
66. Arenkiel, B. R. et al. In vivo light-induced activation of neural circuitry in transgenic mice expressing channelrhodopsin-2. *Neuron* **54**, 205–218 (2007).
67. Boyden, E. S., Zhang, F., Bamberg, E., Nagel, G. & Deisseroth, K. Millisecond-timescale, genetically targeted optical control of neural activity. *Nat. Neurosci.* **8**, 1263–1268 (2005).
68. Lima, S. Q., Hromádka, T., Znamenskiy, P. & Zador, A. M. PINP: a new method of tagging neuronal populations for identification during in vivo electrophysiological recording. *PLoS ONE* **4**, e6099 (2009).
69. Zhang, S.-J. et al. Optogenetic dissection of entorhinal-hippocampal functional connectivity. *Science* https://doi.org/10.1126/science.1232627 (2013).
70. Kvitsiani, D. et al. Distinct behavioural and network correlates of two interneuron types in prefrontal cortex. *Nature* **498**, 363–366 (2013).
71. Stark, E. & Abeles, M. Unbiased estimation of precise temporal correlations between spike trains. *J. Neurosci. Methods* **179**, 90–100 (2009).
72. Buzsáki, G. Theta oscillations in the hippocampus. *Neuron* **33**, 325–340 (2002).
73. Peyrache, A., Khamassi, M., Benchenane, K., Wiener, S. I. & Battaglia, F. P. Replay of rule-learning related neural patterns in the prefrontal cortex during sleep. *Nat. Neurosci.* **12**, 919–926 (2009).
74. van de Ven, G. M., Trouche, S., McNamara, C. G., Allen, K. & Dupret, D. Hippocampal offline reactivation consolidates recently formed cell assembly patterns during sharp wave-ripples. *Neuron* **92**, 968–974 (2016).
75. Williams, C. K. & Rasmussen, C. E. *Gaussian Processes for Machine Learning* Vol. 2 (MIT Press, 2006).
76. Skaggs, W. E., McNaughton, B. L. & Gothard, K. M. in *Advances in Neural Information Processing Systems* 1030–1037 (Morgan Kauffman, 1993).
77. Buzsáki, G. & Mizuseki, K. The log-dynamic brain: how skewed distributions affect network operations. *Nat. Rev. Neurosci.* **15**, 264–278 (2014).

Acknowledgements

We thank A. Fernandez-Ruiz, D. Huilgol, K. McClain, S. McKenzie, A. Navas-Olive, N. Nitzan, M. Valero and I. Zutshi for feedback on an early version of the manuscript. We also thank J. Dasen, Y. Fang, X. Wang, T. Yamaguchi and the Microscopy Laboratory at NYU Langone Health for technical support. This work was supported by grant no. U19NS104590-01and R01 MH122391 (to G.B.).

Author contributions

R.H., H.B. and G.B. designed the study. R.H. and Y.Z. performed the experiments. R.H. performed data analysis and modeling with help from Y.Z. in analyzing histological data. R.H. and G.B. wrote the manuscript with contributions from the other authors.

Competing interests

The authors declare no competing interests.

Additional information

Extended data Extended data are available for this paper at https://doi.org/10.1038/s41593-022-01138-x.

Supplementary information The online version contains supplementary material available at https://doi.org/10.1038/s41593-022-01138-x.

Correspondence and requests for materials should be addressed to Roman Huszár or György Buzsáki.

Peer review information *Nature Neuroscience* thanks Roustem Khazipov and the other, anonymous, reviewer(s) for their contribution to the peer review of this work.

Reprints and permissions information is available at www.nature.com/reprints.

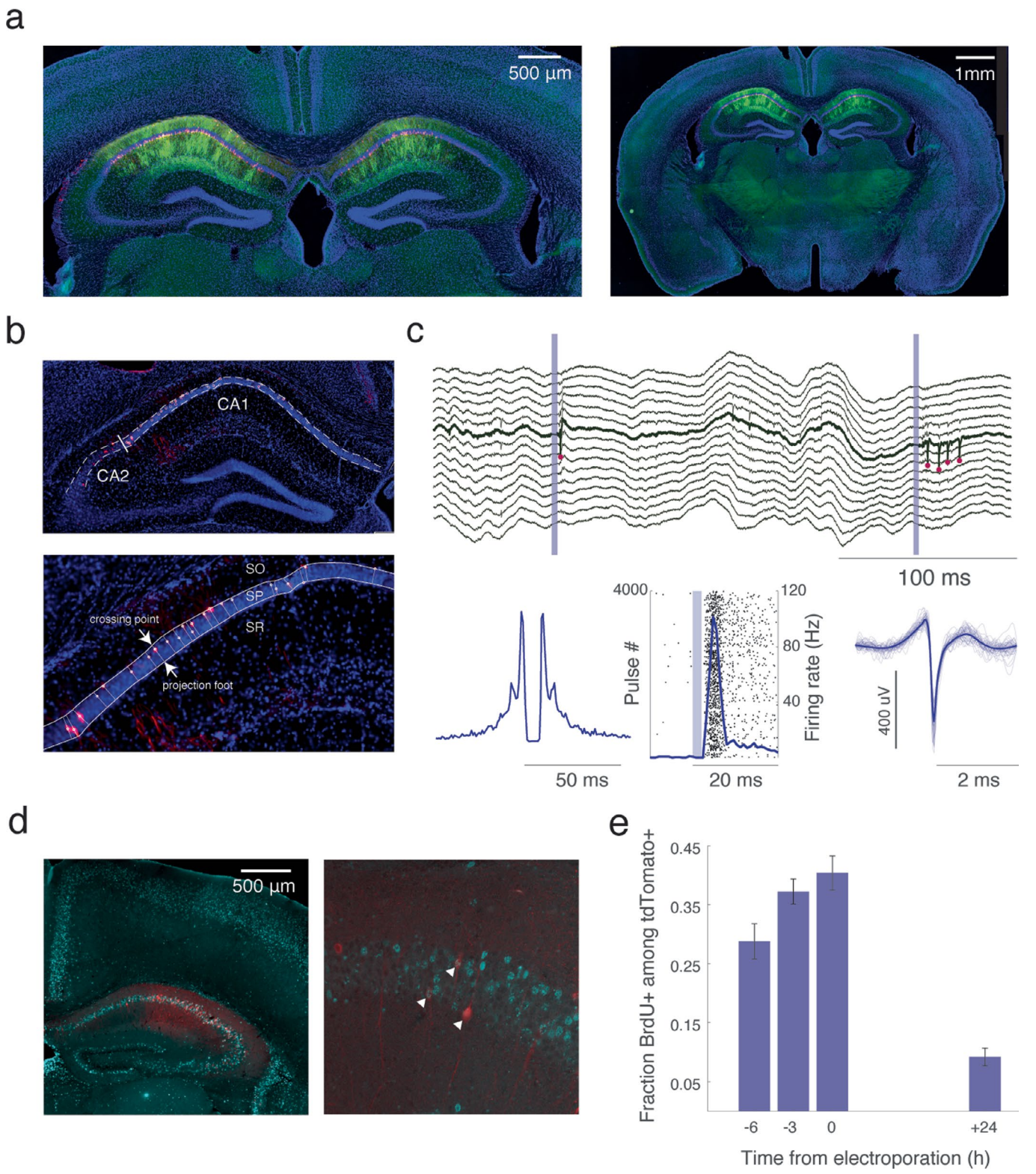

Extended Data Fig. 1 | See next page for caption.

Extended Data Fig. 1 | Birthdating CA1 pyramidal neurons via in utero electroporation. a, Closeup (left) and full view (right) of an example coronal section shows the expression of ChR2-EYFP (green) and tdTomato (red) following in utero electroporation at E15.5. Expression was restricted to the hippocampal CA1 subregion in all n = 17 mice. **b**, Top: tdTomato expression in CA1 following in utero electroporation (different example from **a**). Manually drawn borders (dashed) delimit the pyramidal layer. The border between CA1 and CA2 (thick white line) was approximated by comparing with the Mouse Brain Atlas. White circles: tdTomato+ puncta identified via ImageJ. Bottom: Closeup of the projection foot of each tdTomato+ punctum on the border between stratum pyramidale (SP) and stratum radiatum (SR), from which each neuron's radial depth was computed. Depth was normalized by the distance between the projection foot and crossing point with the border between SP and stratum oriens (SO). **c**, Top: Wideband activity recorded on a single silicon probe shank upon delivery of blue light pulses (2 ms; shaded blue). The bold channel highlights spikes (red dots) of a pyramidal neuron responding to blue light. Bottom: Autocorrelogram (left) of the highlighted neuron's spike train reveals its burst firing, and the PSTH (middle) demonstrates its firing fidelity following light offset. Waveforms of spontaneous spikes are shown on the right (light blue: n = 50 spikes; dark blue: average). **d**, Left: Coronal section showing CA1 expression of tdTomato (red) introduced via in utero electroporation at E15.5. Cyan highlights nuclear expression of 5-bromo-2'deoxyuridine (BrdU), a marker of cell division and a commonly used birthdating tool. Right: A closeup highlighting three CA1 neurons exhibiting both tdTomato and BrdU expression. **e**, Fraction of Brdu and tdTomato double-labeled cells among tdTomato expressing neurons (mean ± SEM) as a function of BrdU injection timing (in hours) with respect to in utero electroporation at time 0. n = 3 animals per timepoint, >300 manually identified tdTomato+ neurons. The largest overlap occurred when BrdU was given at the time of in utero electroporation, whereas minimal overlap was seen when BrdU was injected 24 h after. This suggests that populations electroporated 24 h apart are distinct in terms of embryonic birthdate.

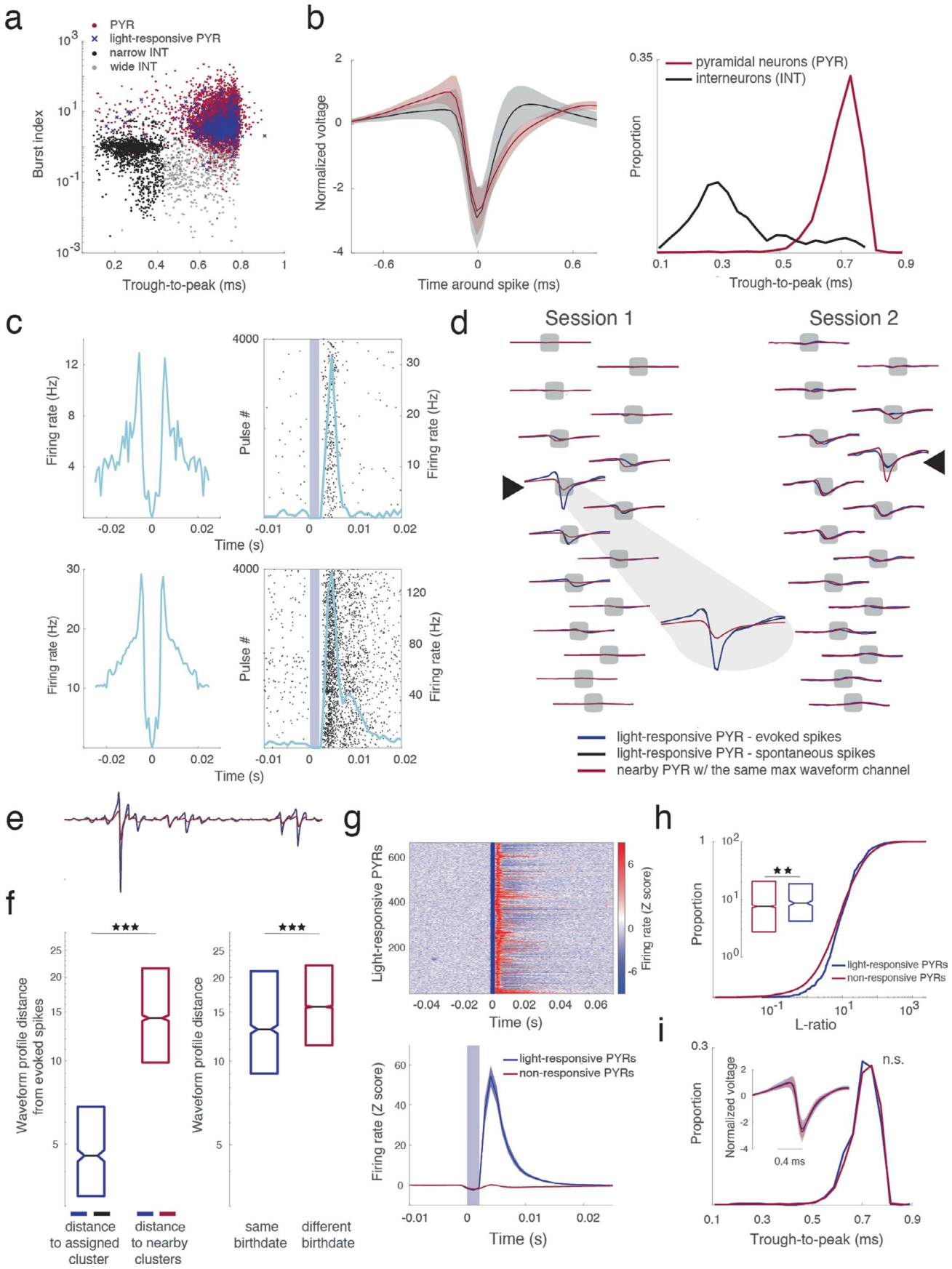

Extended Data Fig. 2 | See next page for caption.

Extended Data Fig. 2 | Clustering, classification and light responsiveness of CA1 neurons. a, Filtered waveform trough-to-peak (ms) by burst index for isolated units ($n = 9,471$). Red: pyramidal neurons ($n = 7,411$). Black: narrow waveform interneurons ($n = 1,556$). Gray: wide waveform interneurons ($n = 504$). Blue crosses: light-responsive pyramidal neurons ($n = 664$, 8.96%). **b**, Left: Filtered waveforms (mean ± SD) of putative pyramidal neurons and interneurons. Right: Trough-to-peak bimodality used for neuron classification. **c**, Examples of light-responsive pyramidal neurons (as in Fig. 1d**)**. **d**, Waveform profiles across recording channels for two neurons with maximum waveform amplitudes occurring on the same channel ('nearby' neurons, black triangle). Two sessions are shown. Blue: evoked spikes (<10 ms following light offset) of a light-responsive pyramidal neuron. Black: same neuron, $n = 1000$ spontaneous out-of-stimulation spikes. Red: non-responsive nearby pyramidal neuron. **e**, Waveforms in **d**, concatenated across channels. The L2 norm of vectorized waveform profile differences was used to quantify waveform profile distance. **f**, Left: Waveform profile distances between evoked and spontaneous spikes of light-responsive pyramidal neurons (blue, median=4.56; $n = 664$) and between evoked and spontaneous spikes of light-responsive and other nearby neurons, respectively (red, median=14.269; $n = 3,086$; P = 1.06e-255; two-sided Wilcoxon). Evoked spikes most resembled spontaneous spikes of their assigned cluster. Right: Waveform profile distances between SBD (blue, median=13.013; $n = 1,743$) and DBD pairs (red, median=15.68; $n = 15,996$; P = 4.6e-27; two-sided Wilcoxon) recorded on the same shank, irrespective of which channel. Only spontaneous spikes were considered. Additional analyses were performed to control for effects of waveform similarity in SBD populations (Extended Data Fig. 10). **g**, Top: PSTHs surrounding light pulse onset for statistically identified light-responsive pyramidal neurons ($n = 664$). Bottom: PSTH mean ± SEM of light-responsive (blue, $n = 664$) and non-responsive pyramidal neurons ($n = 6,747$). **h**, Cluster isolation quality (L-ratio)[63] for light-responsive (blue, median=8.627; $n = 664$) and non-responsive pyramidal neurons (red, median=7.576; $n = 6,747$; P = 4.1e-3; two-sided Wilcoxon). Additional analyses were performed to control for effects of cluster isolation quality in SBD populations (Extended Data Fig. 5). **i**, Waveform shape trough-to-peak (ms) for light-responsive (blue, mean=0.696; $n = 664$) and non-responsive pyramidal neurons (red, mean=0.7; $n = 6,747$; P = 1.34e-1; two-sided, two-sample t-test). Inset: mean ± SD of filtered waveforms. Box plot's central mark, notch and edges indicate the median, its 95% confidence interval, and the 25th/75th percentiles, respectively.

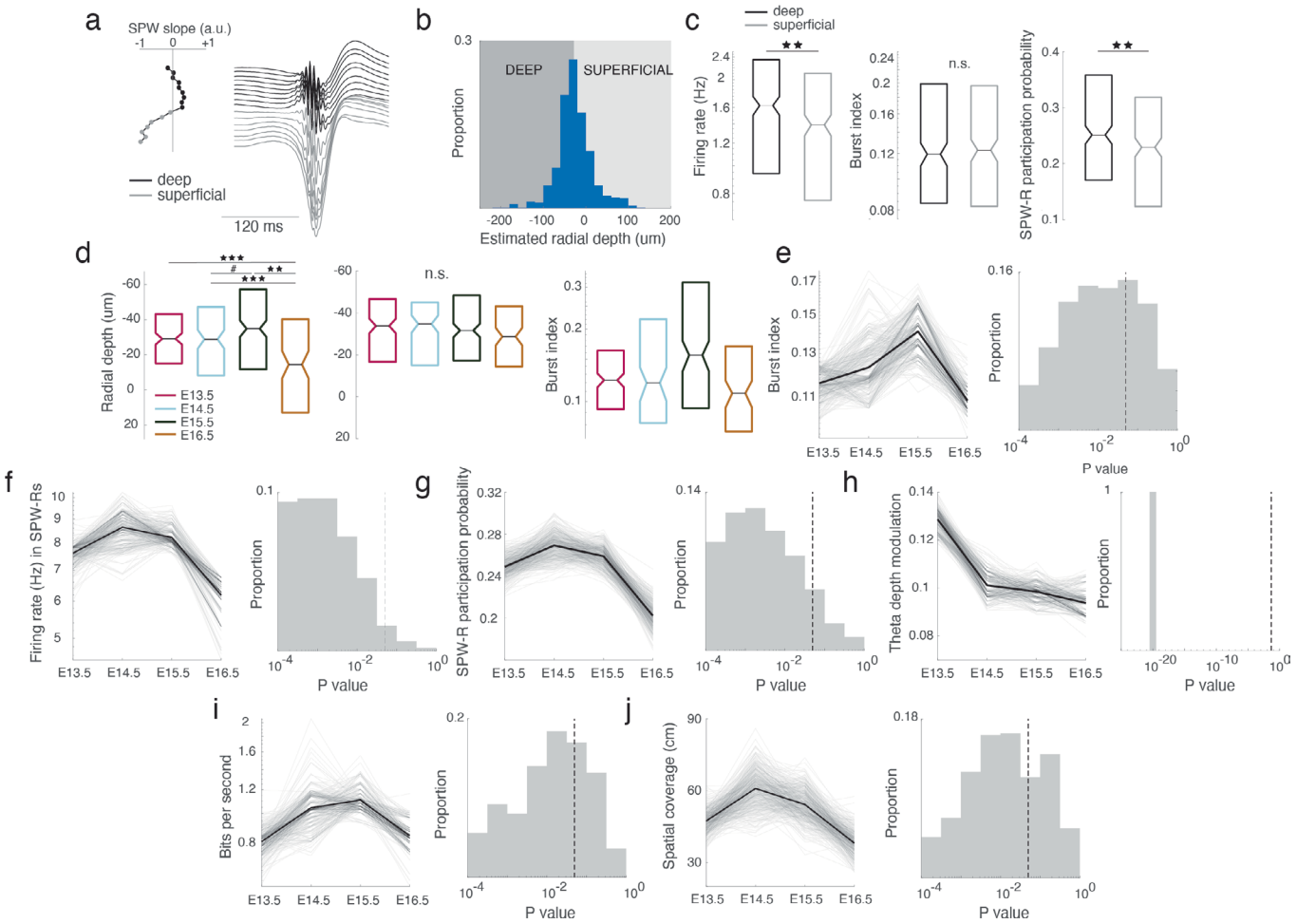

Extended Data Fig. 3 | Birthdate-dependent differences in single cell features cannot be explained by anatomical depth alone. a, LFP profile around SPW-Rs. Sharp wave (SPW) slope estimated radial depth relative to the pyramidal layer center[8,62]. Neuron depth was given by the position of the channel where it exhibited maximal waveform amplitude (Extended Data Fig. 2d). **b**, Median depth of light-responsive pyramidal neurons ($n = 664$) occurred at −28.92 µm relative to SPW reversal. Deep and superficial (Sup) subpopulations were defined by a median-based split of the distribution. **c**, Left: Average firing rate. Deep, median=1.62 Hz ($n = 332$), Sup, median=1.39 Hz ($n = 332$); P = 3.1e-3, two-sided Wilcoxon. Middle: Burst index. Deep, median=0.119 ($n = 332$), Sup, median=0.123 ($n = 332$); P = 8.97e-1, two-sided Wilcoxon. Right: SPW-R participation probability. Deep, median=0.251 ($n = 332$), Sup, median=0.229 ($n = 332$); P = 4.8e-3, two-sided Wilcoxon. **d**, Left: Estimated depth. E13.5, −29 µm ($n = 184$ neurons); E14.5, −28.7 ($n = 132$); E15.5, −34.8 ($n = 233$); E16.5, −14.4 (115). Medians, Kruskal-Wallis: H = 26.327, df=3, P = 0. Middle: Neurons were resampled according to the distribution in **b** to match depth statistics while preserving n. Kruskal-Wallis: H = 3.65, df=3, P = 4.49e-1. Right: Burst indices (Fig. 1h) after matching depth distributions at preserved *n*. Kruskal-Wallis: H = 9.02, df=3, P = 5.2e-2. **e**, The procedure in **d** was repeated $n = 500$ times. Left: Light gray, median burst index across birthdates for each resampling. Black, average across resamplings. Right: P-value distribution (Kruskal-Wallis) across resamplings. Dashed vertical line, P = 0.05. 356/500 (71.2%) depth-matched burst index profiles fell below P = 0.05. Matching depth statistics weakens birthdate-dependent bursting differences, but preserves the bell-shaped profile, suggesting a residual effect of birthdate. **f**, Same as **d**-**e**, for SPW-R-related firing rates (Fig. 2f). 494/500 (98.8%) resamplings were P < 0.05. **g**, Same as **d**-**e**, for participation probability in SPW-Rs (Fig. 2f). 469/500 (93.8%) resamplings were P < 0.05. **h**, Same as **d**-**e**, for theta depth modulation (Fig. 2d). All resamplings were P < 0.05. **i**, Same as **d**-**e**, for spatial information scores (Fig. 5b). 363/500 (72.6%) resamplings were P < 0.05. **j**, Same as **d**-**e**, for spatial coverage (Fig. 5b). 369/500 (73.8%) resamplings were P = 0.05. Box plot central mark, notch and edges indicate the median, its 95% confidence interval, and the 25th/75th percentiles, respectively.

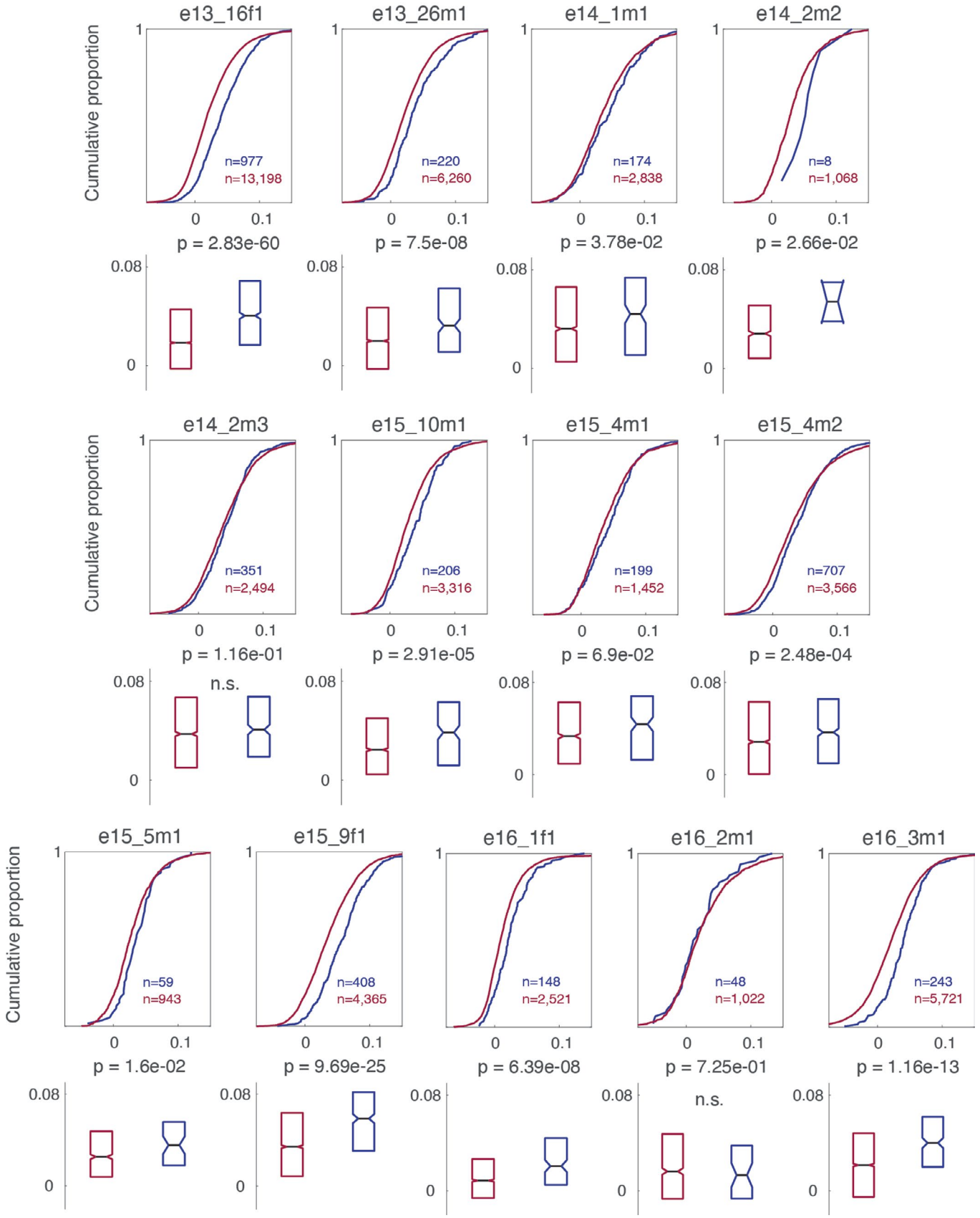

Extended Data Fig. 4 | See next page for caption.

Extended Data Fig. 4 | SPW-R correlations for pyramidal neuron pairs in individual mice. Cumulative distributions and box plot summaries of pairwise correlations in SPW-Rs for pairs of SBD (blue) and DBD (red) neurons in individual animals. SBD pyramidal neurons exhibited higher cofiring in SPW-Rs than DBD pairs in 11/13 animals. Group sizes and P-values of two-sided Wilcoxon tests are shown above each box plot summary. Two animals electroporated at E13.5 were excluded due to a lack of SBD pairs. In these two mice only a single light-responsive pyramidal neuron per session was recorded. Box plot central mark, notch and edges indicate the median, its 95% confidence interval, and the 25th/75th percentiles, respectively.

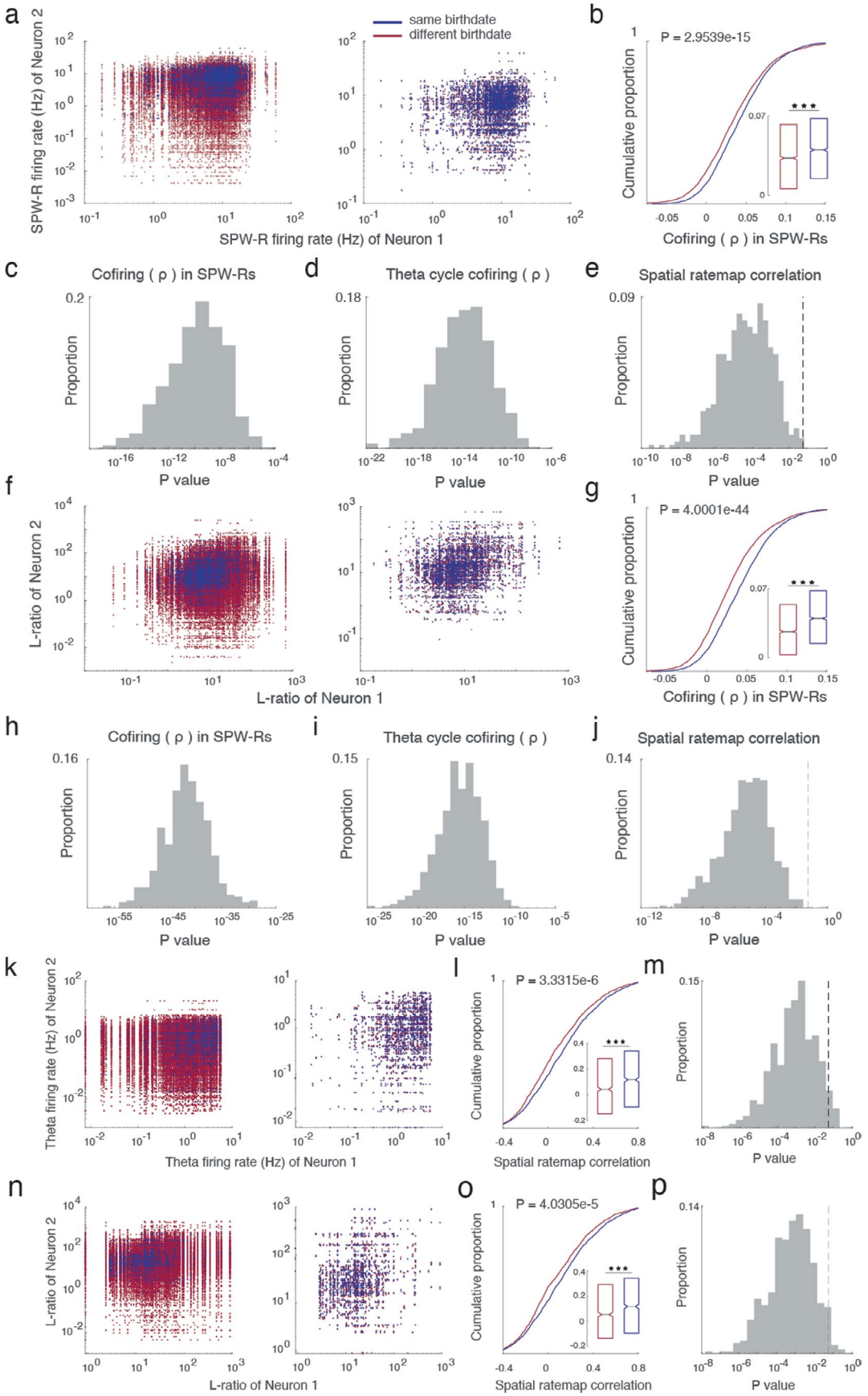

Extended Data Fig. 5 | See next page for caption.

Extended Data Fig. 5 | Matching firing rate and L-ratio statistics supports results in Fig. 2c,g, Fig. 5c and Fig. 6e. a, Left: Firing rate in SPW-Rs for SBD (blue, $n = 3{,}751$) and DBD (red, $n = 50{,}461$) pairs that contributed to pairwise correlation analyses in Fig. 2g. Right: Resampling the distribution of DBD pairs according to the empirical probability mass function of SBD pairs matches pairwise firing rate statistics and group sizes. **b**, Cofiring in SPW-Rs for SBD (blue, $n = 3{,}751$) and resampled DBD pairs (red, $n = 3{,}751$; $P = 2.95e\text{-}15$, two-sided Wilcoxon). **c**, Two-sided Wilcoxon P-values ($n = 500$ resamplings) for the comparison in **b**. All tests were $P < 0.05$. **d**, Same as **a**-**c** for theta cycle correlations (Fig. 2c) after $n = 500$ resamplings matching theta-related firing rates. All tests were $P < 0.05$. **e**, Same as **a**-**c** for spatial ratemap correlations (Fig. 5c) after $n = 500$ resamplings matching theta-related firing rates. 499/500 (99.8%) tests were $P < 0.05$. **f**, The same resampling as **a** matching L-ratio cluster isolation between SBD (blue, $n = 3{,}751$) and DBD (red, $n = 50{,}461$) pairs. **g**, Cofiring in SPW-Rs for SBD (blue, $n = 3{,}751$) and resampled DBD pairs (red, $n = 3{,}751$; $P = 4.0001e\text{-}44$, two-sided Wilcoxon). **h**, Two-sided Wilcoxon P-values ($n = 500$ resamplings) for the comparison in **g**. All P-values were < 0.05. **i-j**, Same as **f**-**h** for theta cycle (**i**) and spatial ratemap (**j**) correlations after $n = 500$ resamplings matching L-ratio statistics. All P-values were < 0.05. **k**, The same resampling as **a** matching theta-related firing rates of SBD (blue, $n = 1{,}510$) and DBD (red, $n = 50{,}461$) pairs that contributed to novel environment-related spatial ratemap correlations (Fig. 6e**)**. **l**, Novel environment-related spatial ratemap correlations for SBD (blue, $n = 1{,}510$) and resampled DBD pairs (red, $n = 1{,}510$; $P = 3.3e\text{-}6$ two-sided Wilcoxon). **m**, Two-sided Wilcoxon P-values ($n = 500$ resamplings) for the comparison in **l**. 479/500 (95.8%) tests were $P < 0.05$. **n**-**p**, Same as **k**-**m** matching L-ratio cluster isolation statistics. **p**, 487/500 (97.4%) tests were $P < 0.05$. These results demonstrate that differences shown in Fig. 2c, g, Fig. 5c and Fig. 6e cannot be explained by firing rate, cluster isolation, or group size differences. Vertical dashed line indicates $P = 0.05$. Box plot central mark, notch and edges indicate the median, its 95% confidence interval, and the 25th/75th percentiles, respectively.

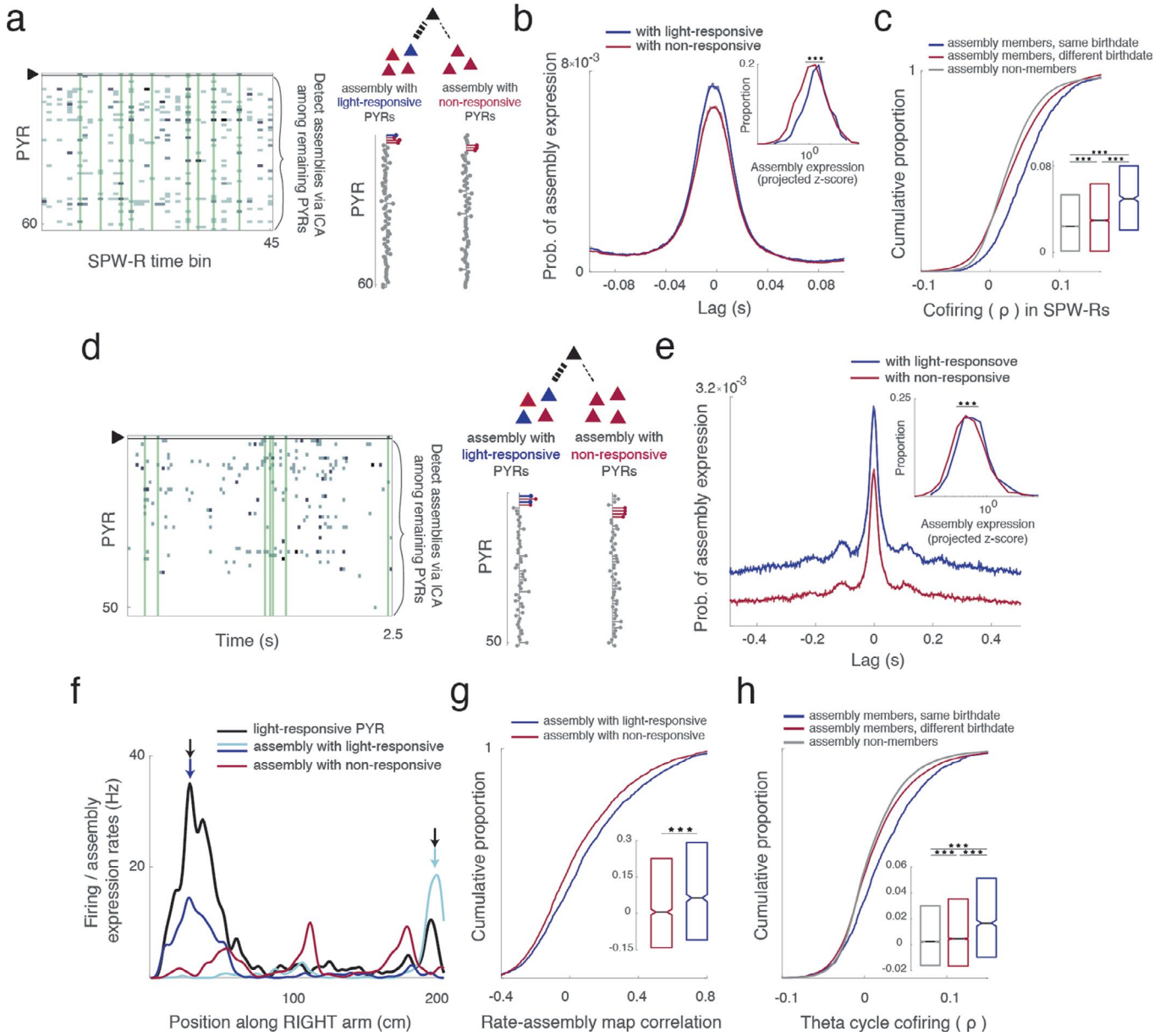

Extended Data Fig. 6 | Birthdated pyramidal cells join assemblies comprising other SBD neurons. a, Left: Raster plot illustrating conditional assembly detection during SPW-R-related spiking. SPW-Rs were binned at 25 ms resolution and concatenated. Assemblies were detected around spikes of a held-out, light-responsive pyramidal neuron (black triangle), with ICA performed on the remaining pyramidal neurons in time windows surrounding the held-out neuron's spikes (vertical green bars). Right: Example independent components. Assembly members were determined as in Fig. 3. Assemblies with light-responsive members (blue, left) were compared to those consisting exclusively of non-responsive members (red, right). **b**, Probability of assembly expression around SPW-R-related spikes of the held-out neuron. Inset, Assembly expression strength at the time of the held-out neuron's spike (blue, median=1.38, $n=1{,}109$; red, median=1.235, $n=2{,}747$; P = 2.29e-11; two-sided Wilcoxon). **c**, Pairwise spike count correlations in SPW-Rs between each held-out neuron and its SBD assembly members (blue, median=0.05, $n=1{,}153$), DBD assembly members (red, median=0.0296, $n=15{,}906$) and assembly non-members (gray, median=0.0242, $n=37{,}947$). Kruskal-Wallis: H = 342.63, df=2, P = 0. **d**, Conditional assembly detection (as in **a**) during behavior on the familiar figure-eight maze (2.5 s binning). Right: Example independent components. **e**, Probability of assembly expression around spikes of the held-out neuron. Inset, Assembly expression strength at the time of the held-out neuron's spike (blue, median=0.73, $n=1{,}705$; red, median=0.663, $n=2{,}529$; P = 9.9e-13; two-sided Wilcoxon). **f**, Spatial firing ratemap of a held-out, light-responsive pyramidal neuron (black), and assembly expression ratemaps of assemblies with light-responsive (dark and light blue) and non-responsive (red) members. Arrows, overlapping place fields. **g**, Correlations between held-out neurons' ratemaps and assembly expression ratemaps for assemblies with light-responsive (blue, median=0.064; $n=1705$) and non-responsive members (red, median=0.0057; $n=2529$; P = 1.13e-08 two-sided Wilcoxon). **h**, Pairwise spike count correlations in theta cycles between each held-out neuron and its SBD assembly members (blue), DBD assembly members (red), and assembly non-members (gray). w/ SBD members, 0.0166 ($n=1611$); w/ DBD members, 0.0046 ($n=18650$); w/ non-members, 0.0023 ($n=25374$). Medians, Kruskal-Wallis: H = 153.4885, df=2, P = 0. ***P < 0.001. Box plot central mark, notch and edges indicate the median, its 95% confidence interval, and the 25th/75th percentiles, respectively.

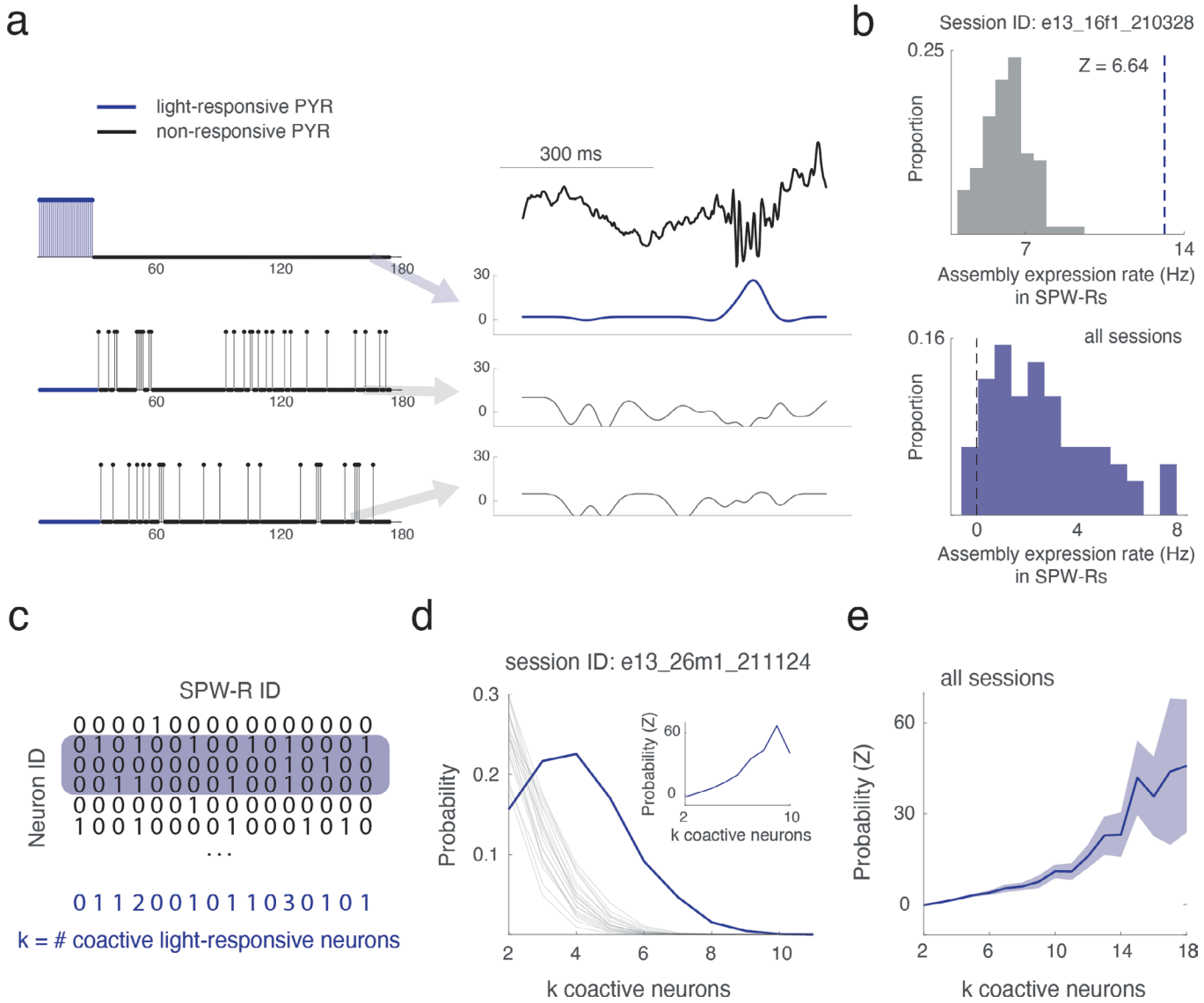

Extended Data Fig. 7 | Expression of assemblies comprising exclusively SBD pyramidal neurons. a, Left: Hard-coded weights define assemblies of different pyramidal neuron subgroups in an example session. This approach complements Fig. 3 where weights are assigned in an unsupervised manner via ICA. Blue: light-responsive neurons, black: non-responsive neurons. Top vector, assembly of light-responsive neurons ($n = 27$ members). Bottom two vectors, equal-sized assemblies with members randomly drawn from the non-responsive population ($n = 147$ in this session). Right: Time-resolved assembly expression during a SPW-R, obtained as in Fig. 3d. Significant peaks were taken as timepoints of assembly expression (Methods). **b**, Top: In an example session, SPW-R-related assembly expression rate (Hz) for an assembly consisting exclusively of light-responsive members (dashed blue) and for assemblies comprising randomly selected equal-sized subsets of non-responsive members ($n = 100$ groupings, gray histogram). The expression rate of the assembly comprising light-responsive members was expressed as a Z-score with respect to this distribution. Bottom: Z-scored expression rates of assemblies of light-responsive members across all sessions with ≥3 light-responsive pyramidal neurons. 62/65 (95.38%) values fell above zero, suggesting a greater propensity for higher order coactivation in assemblies of light-responsive members compared to equal-sized control assemblies. **c**, SPW-R-related firing of pyramidal neurons was binarized in each session. Instances of multiple spikes per SPW-R event were still recorded as '1'. For each SPW-R, the number of coactive light-responsive neurons (blue) was calculated. **d**, Probability of observing exactly k coactive (out of $n = 11$) light-responsive neurons (blue) in an example session. As control, random equal-sized subgroups of non-responsive neurons ($n = 145$ in this session) were selected, and the probability of k coactive neurons in SPW-Rs was computed. This was performed 1000 times (20 example traces are shown in gray), yielding a null distribution of probabilities for each k. Inset, Probability of k coactive light-responsive neurons expressed as a Z-score with respect to the null distribution. **e**, SPW-R-related probability of k-coactive light-responsive neurons (Z-scored; mean ± SEM) across all recording sessions with at least 2 light-responsive pyramidal neurons ($n = 84$ sessions). Light-responsive neurons of the same birthdate tend to coactivate in subgroups of more than 2 neurons.

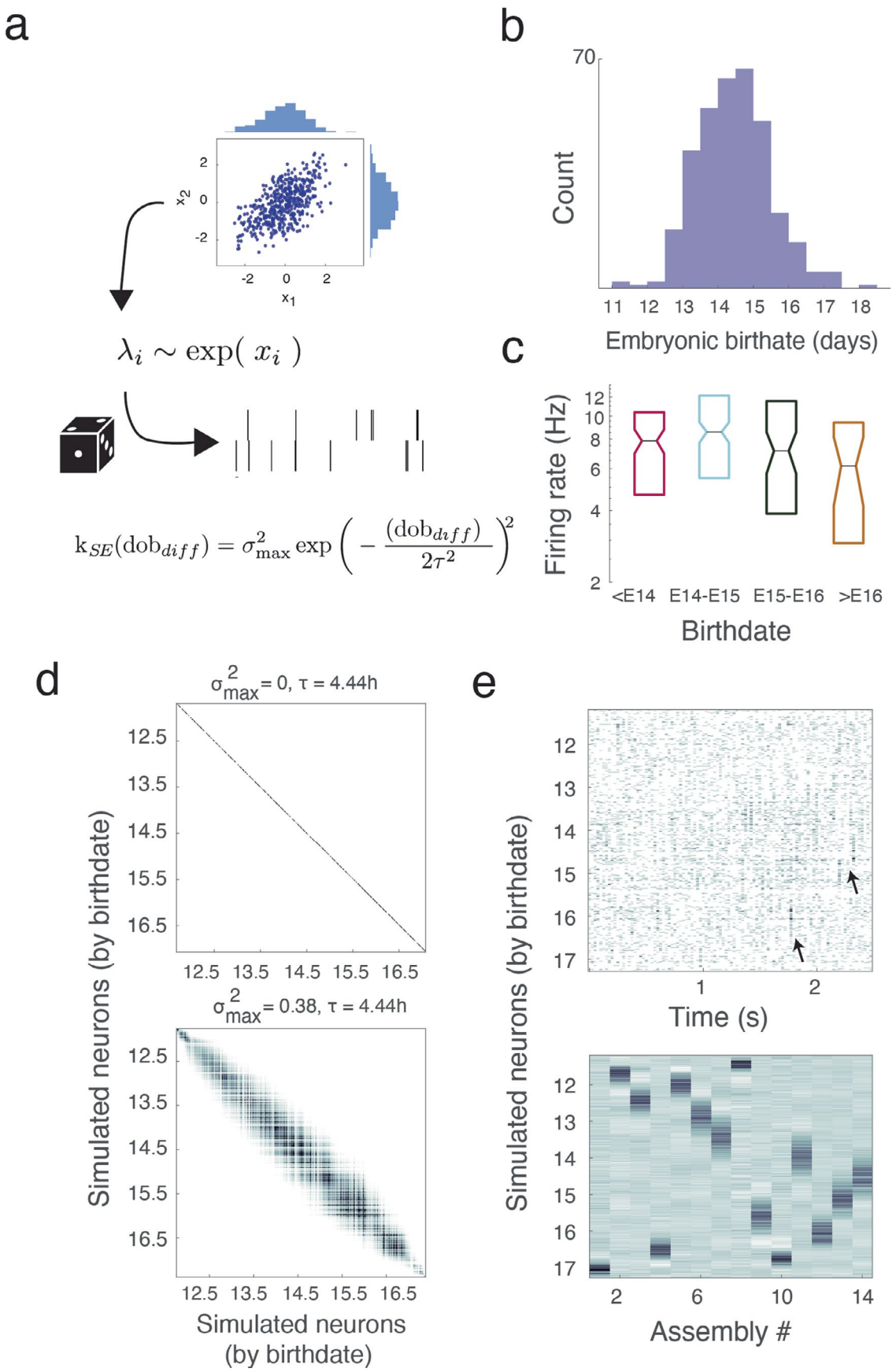

Extended Data Fig. 8 | See next page for caption.

Extended Data Fig. 8 | Linear-nonlinear Poisson model for exploring assembly dynamics. a, Schematic illustrating the linear-nonlinear Poisson model. A multivariate Gaussian distribution $\boldsymbol{x}$ with predefined mean and covariance was transformed using an exponential nonlinearity. The resulting lognormally distributed process λ was taken as the rate of a Poisson process to generate spike trains. $k_{sE}(dob_{diff})$ is the kernel function for the Gaussian covariance, and depends on the difference of birthdates (dob_{diff}) between simulated neurons. **b**, Distribution of simulated birthdates of $n = 350$ neurons. Birthdates were sampled from a Gaussian with mean birthdate (E)14.5, and standard deviation of 1 day. **c**, Average firing rates of simulated neurons were set according to empirically observed firing rate distributions in SPW-Rs (Fig. 2f). <E14, $n = 107$; E14-E15, $n = 68$; E15-E16, $n = 71$; >E16, $n = 104$. **d**, Analytical covariance matrices ($Cov\ (\lambda_i \lambda_j)$) for two values of σ^2_{max}, and a fixed value τ. These values were identical to the examples of simulated assembly expression rates in Fig. 4c. **e**, Simulated raster plot (top) and extracted assembly independent components (bottom) with kernel parameters $\sigma^2_{max} = 0.38$ and τ=4.44h. Arrows in the raster plot point to observable assembly expressions. Box plot central mark, notch and edges indicate the median, its 95% confidence interval, and the 25th/75th percentiles, respectively.

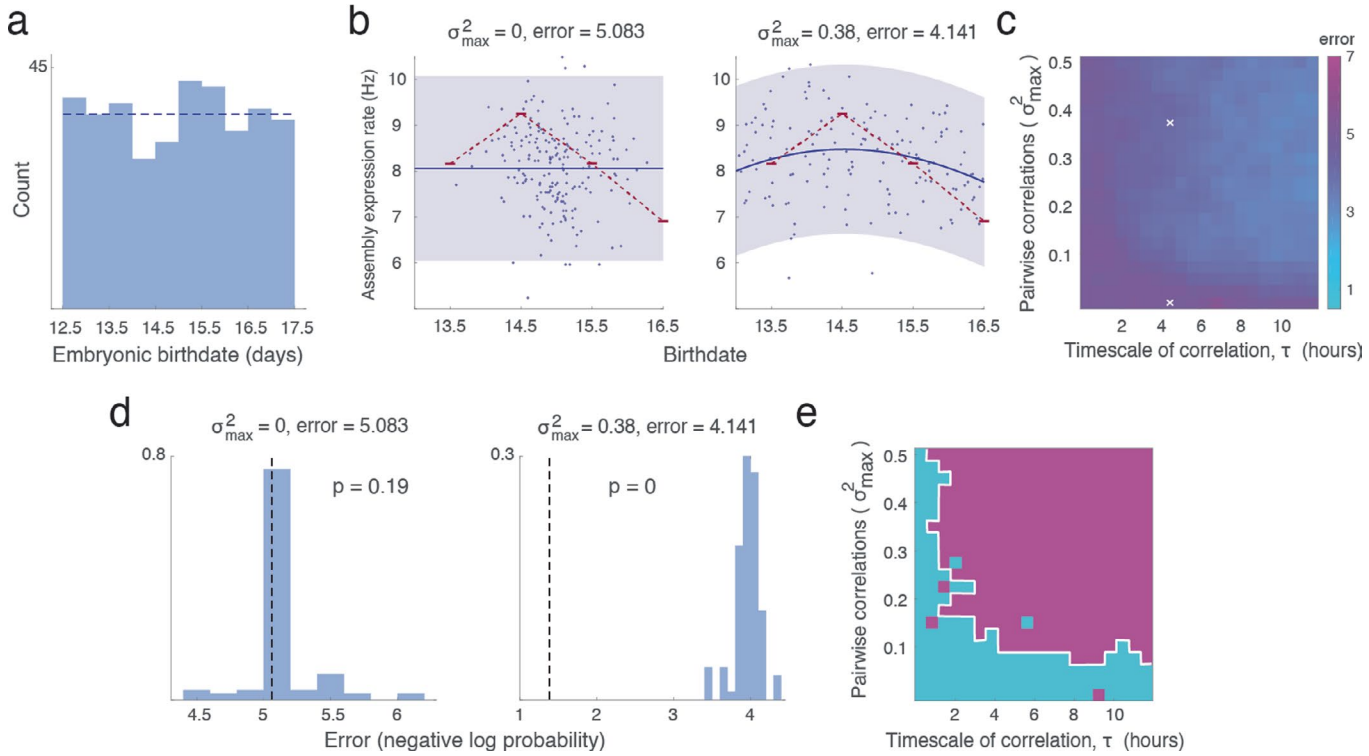

Extended Data Fig. 9 | Uniform rate of neurogenesis fails to capture bell-shaped assembly dynamics. a, Distribution of simulated birthdates of $n = 350$ neurons, sampled from a uniform distribution. **b**, Simulated assembly expression rates at different birthdates (blue dots) and their fit to assembly expression rates observed in data (red, average from Fig. 3e) depending on correlation strength σ^2_{max} between SBD neurons (same as Fig. 4c). **c**, Negative log probability (error) matrix quantifying goodness-of-fit of the uniform model (same color scale as Fig. 4d). White crosses show examples from **b**. **d**, Histogram of $n = 100$ error values obtained under the two parameter regimes highlighted in **b**. Each value was obtained from an independent sampling of the uniform model. Dashed vertical lines indicate the error under the bell-shaped model from Fig. 4. Single-tailed P-values were defined as the fraction of uniform model-generated error values that are smaller than the bell-shaped model-generated error for the same set of parameters. **e**, Matrix of thresholded P-values (as described in **d**) for the full range of model parameters. Magenta: $P < 0.05$; cyan: $P > 0.05$. The white line highlights a separation in the parameter space where the bell-shaped model performs no better than the uniform model (bottom left), and where the bell-shaped model outperforms the uniform (upper right).

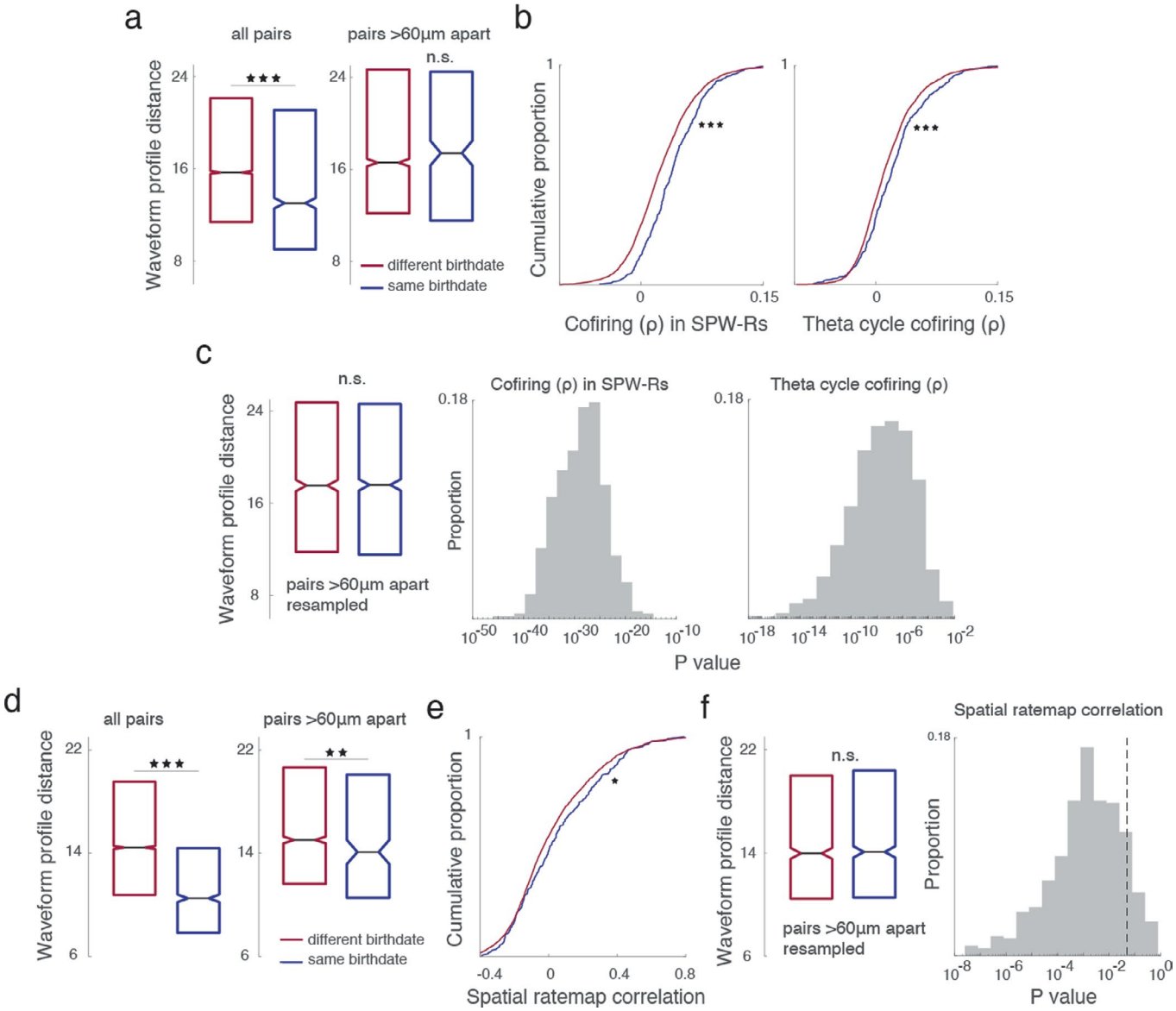

Extended Data Fig. 10 | Matching of waveform profile distances supports results in main Fig. 2c, g and Fig. 5c. a, Left: Waveform profile distances (Extended Data Fig. 2d-f) for SBD (blue, median=13.0128, *n*=1,743) and DBD same-shank pairs (red, median=15.68, *n*=15,996; P=4.6e-27) contributing to analyses in Fig. 2c, g. Right: Waveform profile distances for same-shank pairs recorded >60 µm apart. Blue: median=17.41, *n*=347. Red, median=16.59, *n*=3,581. P=5.5e-1. Anatomical distance was defined as the distance between the neurons' maximum waveform channels on the probe layout. Same-shank SBD and DBD pairs recorded >60 µm apart were less differentially affected by spike sorting errors, as evidenced by similar waveform profile distances. **b**, Left: SPW-R-related pairwise correlations (Fig. 2g) of same-shank SBD (blue, median=0.037, *n*=347) and DBD (red, median=0.021, *n*=3,588; P=1.4e-04) pairs recorded >60 µm apart. Right: Theta cycle correlations (Fig. 2c) for pairs shown on the left. Blue: SBD, median=0.019. Red: DBD, median=0.0092. P=4.3e-12. **c**, Left: Waveform profile distances of DBD pairs recorded >60 µm apart were resampled according to the empirical probability mass function of waveform profile distances of SBD pairs. Group size was fixed at *n*=1,743 of the original SBD group. >60 µm SBD pairs were sampled with replacement to achieve the latter. Blue: median=17.5854. Red: DBD, median=17.5305. P=6.9e-1. Right: P-value distribution (*n*=500 resamplings) for comparisons shown in **b**. All tests were P < 0.05. **d**, Same as **a** for same-shank pairs involved in spatial ratemap correlation analyses in Fig. 5c. Left: Blue: SBD, median=10.498, *n*=1,205. Red: DBD, median=14.49, *n*=13,549. P=6.5e-107. Right: Blue: SBD, median=14.0836, *n*=252. Red: DBD, median=15.028, *n*=2,998. P=7.8e-3. **e**, Spatial ratemap correlation of same-shank pairs recorded >60 µm apart. Blue: SBD, median=0.0079, *n*=252. Red: DBD, median=−0.0308, *n*=2998. P=3.3e-2. **f**, Same resampling as **c** matching waveform profile distances and group sizes of pairs involved in the spatial ratemap correlation analysis in Fig. 5c. Blue: SBD, median=14.0856. Red: DBD, median=13.97. P=3.1e-1. Right: P-value distribution (*n*=500 resamplings) for the comparison in **e**. 447/500 (89.4%) tests were P < 0.05. Vertical dashed line indicates P=0.05. Group comparisons were based on a two-sided Wilcoxon test. Box plot central mark, notch and edges indicate the median, its 95% confidence interval, and the 25th/75th percentiles, respectively.

nature portfolio

Corresponding author(s): György Buzsáki

Last updated by author(s): Jul 6, 2022

Reporting Summary

Nature Portfolio wishes to improve the reproducibility of the work that we publish. This form provides structure for consistency and transparency in reporting. For further information on Nature Portfolio policies, see our Editorial Policies and the Editorial Policy Checklist.

Statistics

For all statistical analyses, confirm that the following items are present in the figure legend, table legend, main text, or Methods section.

n/a	Confirmed
☐	☒ The exact sample size (*n*) for each experimental group/condition, given as a discrete number and unit of measurement
☐	☒ A statement on whether measurements were taken from distinct samples or whether the same sample was measured repeatedly
☐	☒ The statistical test(s) used AND whether they are one- or two-sided *Only common tests should be described solely by name; describe more complex techniques in the Methods section.*
☐	☒ A description of all covariates tested
☐	☒ A description of any assumptions or corrections, such as tests of normality and adjustment for multiple comparisons
☐	☒ A full description of the statistical parameters including central tendency (e.g. means) or other basic estimates (e.g. regression coefficient) AND variation (e.g. standard deviation) or associated estimates of uncertainty (e.g. confidence intervals)
☐	☒ For null hypothesis testing, the test statistic (e.g. *F*, *t*, *r*) with confidence intervals, effect sizes, degrees of freedom and *P* value noted *Give P values as exact values whenever suitable.*
☒	☐ For Bayesian analysis, information on the choice of priors and Markov chain Monte Carlo settings
☐	☒ For hierarchical and complex designs, identification of the appropriate level for tests and full reporting of outcomes
☐	☒ Estimates of effect sizes (e.g. Cohen's *d*, Pearson's *r*), indicating how they were calculated

Our web collection on statistics for biologists contains articles on many of the points above.

Software and code

Policy information about availability of computer code

Data collection	Neural data was collected using Intan amplifier boards (RHD2132/RHD2000 Evaluation System, Intan) and visualized using the Neurosuite software. Light pulse waveforms for optogenetics were generated using the Cyclops library available for Arduino/Teensy (https://github.com/jonnew/cyclops). Animal tracking was performed using a Basler camera (acA1300-60 gmNIR, Graftek Imaging). Images were acquired using a fluorescent (LEICA VT10000 S) and confocal (Zeiss LSM 800) microscopes.
Data analysis	Custom lab software is available at https://github.com/buzsakilab/buzcode (LFP extraction/downsampling, state scoring, SPW-R detection, phase analysis, monosynaptic connection detection, ICA analysis). Automated spikesorting was performed using Kilosort1, followed by manual curation in Phy2. Unit classification was performed using CellExplorer (https://cellexplorer.org). Gaussian process regression was performed using the GPML toolbox (http://www.gaussianprocess.org/gpml/code/matlab/doc/). Microscopic images were analyzed using custom scripts written in ImageJ (https://imagej.nih.gov/ij/). Custom scripts for data analysis are available at https://github.com/rhuszar.

For manuscripts utilizing custom algorithms or software that are central to the research but not yet described in published literature, software must be made available to editors and reviewers. We strongly encourage code deposition in a community repository (e.g. GitHub). See the Nature Portfolio guidelines for submitting code & software for further information.

Data

Policy information about availability of data

All manuscripts must include a data availability statement. This statement should provide the following information, where applicable:

- Accession codes, unique identifiers, or web links for publicly available datasets
- A description of any restrictions on data availability
- For clinical datasets or third party data, please ensure that the statement adheres to our policy

The dataset generated for the current study is made publicly available in the Buzsaki lab data repository (https://buzsakilab.nyumc.org/datasets/).

Field-specific reporting

Please select the one below that is the best fit for your research. If you are not sure, read the appropriate sections before making your selection.

☒ Life sciences ☐ Behavioural & social sciences ☐ Ecological, evolutionary & environmental sciences

For a reference copy of the document with all sections, see nature.com/documents/nr-reporting-summary-flat.pdf

Life sciences study design

All studies must disclose on these points even when the disclosure is negative.

Sample size	n=17 mice were used (male and female), with the following subgroup sizes: n=4 (E13.5), n=3 (E14.5), n=6 (E15.5), n=4 (E16.5). These sample sizes are standard in the field of high density recordings from behaving animals: e.g., Grosmark and Buzsaki 2016, McKenzie et al 2021.
Data exclusions	Two mice were excluded for analyses involving pairwise statistics of neuronal cofiring at the level of individual animals (Fig. 2G and Extended Data Fig. 4). This was due to a lack of pairs of birthdated neurons, as only a single birthdated neuron was recorded at a time.
Replication	The main result of the present study (cofiring of same birthdate neurons) holds robustly at the level of individual animals (Fig. 2G and Extended Data Fig. 4).
Randomization	Animals were allocated to groups based on the embryonic stage (E13.5, E14.5, E15.5, or E16.5) at which their CA1 neurons were transfected. As such, grouping was part of the experimental design. Control analyses were performed to control for confounding variables of correlated firing such as firing rate, cluster isolation quality, and waveform similarity (Extended Data Fig 5,10).
Blinding	The first author of the study was solely responsible for preparing the groups of mice (in-utero electroporation at different birthdates), as well as maintaining the colony, and all subsequent experiments. As such, blinding was not possible in this study.

Reporting for specific materials, systems and methods

We require information from authors about some types of materials, experimental systems and methods used in many studies. Here, indicate whether each material, system or method listed is relevant to your study. If you are not sure if a list item applies to your research, read the appropriate section before selecting a response.

Materials & experimental systems

n/a	Involved in the study
☐	☒ Antibodies
☒	☐ Eukaryotic cell lines
☒	☐ Palaeontology and archaeology
☐	☒ Animals and other organisms
☒	☐ Human research participants
☒	☐ Clinical data
☒	☐ Dual use research of concern

Methods

n/a	Involved in the study
☒	☐ ChIP-seq
☒	☐ Flow cytometry
☒	☐ MRI-based neuroimaging

Antibodies

Antibodies used	Primary: anti-BrdU (1:250; OriGene TA190126; clone OTI4C2) and anti-RFP (1:500; Rockland 600-401-379). Secondary: anti-rat AlexaFluor647 (1:500; ThermoFisher A-21247) and anti-rabbit AlexaFluor488 (1:500; ThermoFisher A-11008).
Validation	rabbit anti-RFP and anti-rabbit antibodies amplified an endogenously fluorescent tdTomato protein; strong overlap of these two signals (tdTomato in red and anti-rabbit in green) in n=2 control brains was taken as in-house validation of the anti-RFP antibody. Brdu antibody was validated for IHC by the manufacturer (https://www.thermofisher.com/antibody/product/BrdU-Antibody-clone-OTI4C2-Monoclonal/TA190126).

Animals and other organisms

Policy information about studies involving animals; ARRIVE guidelines recommended for reporting animal research

Laboratory animals	Species: Mice; Strain: C57BL/6; Sex: n=12 male, n=5 female; Ages between 3-6 months. Housing conditions: reverse cycle. Temperature: 72+/-2 °F. Humidity: 30-70%.
Wild animals	No wild animals were used in the study.
Field-collected samples	No field collected samples were used in the study.
Ethics oversight	All experiments were conducted in accordance with the Institutional Animal Care and Use Committee of New York University Medical Center (IA15-01466).

Note that full information on the approval of the study protocol must also be provided in the manuscript.